

## Chapter 7

### Frequency-domain techniques for tissue spectroscopy and imaging

S. Fantini and M. A. Franceschini

*Bioengineering Center, Dept. of Electrical Engineering and Computer Science,  
Tufts University, 4 Colby Street, Medford, MA 02155*

#### Contents

##### 7.1 Introduction

##### 7.2 Instrumentation, modulation methods, and signal detection

7.2.1 Lasers and arc lamps

7.2.2 Pulsed sources

7.2.3 Laser diodes and light emitting diodes (LED's)

7.2.4 Optical detectors

7.2.5 Heterodyne detection, digital signal processing, and Fourier filtering

7.2.6 A frequency-domain tissue spectrometer

##### 7.3 Modeling light propagation in scattering media

7.3.1 The Boltzmann transport equation (BTE)

7.3.2 Expansion of the Boltzmann equation in spherical harmonics

7.3.3 The  $P_N$  approximation

7.3.4 The  $P_1$  approximation

7.3.5 The reduced scattering coefficient

7.3.6 The  $P_1$  equation and the standard diffusion equation (SDE)

7.3.7 Solution of the standard diffusion equation in the frequency-domain

##### 7.4 Tissue spectroscopy and oximetry

7.4.1 Optical properties of biological tissue

7.4.1.1 Absorption

7.4.1.2 Scattering

7.4.2 Absorption spectroscopy of tissues

7.4.3 Near-infrared tissue oximetry

7.4.4 Measurements of optical scattering in tissues

##### 7.5 Optical imaging of tissues

7.5.1 General concepts

7.5.2 Non-invasive optical imaging of the human brain

7.5.2.1 Detection of intracranial hematomas

7.5.2.2 Functional imaging of the brain

7.5.3 Optical mammography

##### 7.6 Future directions

## 7.1 Introduction

In frequency-domain spectroscopy, the intensity of the light source is sinusoidally modulated at a frequency  $f$ . One can fully describe the modulated intensity using three parameters, namely the average intensity (DC intensity), the amplitude of the intensity oscillations (AC amplitude), and the phase ( $\Phi$ ) of the intensity wave. The modulation is defined by the ratio AC/DC. Because the phase measurement and the intensity modulation are the key features of frequency-domain spectroscopy, the term *phase-modulation* is sometimes used interchangeably with *frequency-domain*. The phase measurement is related to the time-delay experienced by the probing intensity-wave. If  $\tau$  is a typical time delay, the phase is of the order of  $\omega\tau$ , where  $\omega = 2\pi f$  is the angular modulation frequency. To obtain phase measurements with good signal-to-noise ratio, it is required that  $\omega\tau \sim 1$ , which is the condition that guides the choice of the modulation frequency,  $f$ . In the case of near-infrared spectroscopy and imaging of tissues,  $\tau \sim 1$  ns for source-detector separations on the order of a few centimeters.<sup>1,2</sup> Consequently, the condition  $\omega\tau \sim 1$  determines  $f \sim 100$  MHz, which falls within the radio-frequency range. The 100 MHz frequency range is the one typically used for frequency-domain optical studies of biological tissues.

In this chapter, we describe the frequency-domain instrumentation (section 7.2), the theoretical modeling of light propagation in tissue (section 7.3), and *in vivo* applications of frequency-domain spectroscopy (section 7.4) and imaging (section 7.5). We have tried to make this chapter self-contained, while providing extensive reference to the literature as a guide for additional reading and for in depth coverage of topics that are only briefly mentioned here due to space considerations.

## 7.2 Instrumentation, modulation methods, and signal detection

Frequency-domain spectroscopy can be implemented using several instrumental schemes. For instance, homodyne techniques [in phase-quadrature (IQ), or zero-cross detection] perform amplitude and phase measurements without down-converting the radio frequency, while heterodyne detection (using two oscillators) relies on down conversion of the radio frequency from the 100 MHz range to the kHz range. Furthermore, signal processing may involve zero crossing detectors and analog filters, or analog-to-digital conversion and Fourier filters. A comprehensive review of the instrumentation for optical studies of tissue in the frequency-domain can be found in Ref. 3. In sections 7.2.1-7.2.5, we describe the various light sources and modulation methods, and the principles of heterodyne detection with digital signal processing and Fourier filtering. In section 7.2.6, we describe a specific frequency-domain instrument for near-infrared tissue spectroscopy.

### 7.2.1 Lasers and arc lamps

The emission of continuous-wave lasers and arc lamps can be modulated using devices based on the electro-optical (Pockels cells)<sup>4</sup> or acousto-optical<sup>5,6</sup> effect. A Pockels cell is a birefringent crystal whose indices of refraction can be varied by applying an electric field. The application of a time-varying voltage to the Pockels cell modulates the relative phase delay of the light components polarized along the two principal axes of the cell. If this relative phase delay, or retardation, oscillates between 0 and  $\pi$ , when the modulated Pockels cell is sandwiched between two crossed linear polarizers, each at an angle of  $45^\circ$  with respect to the principal axes of the cell, one achieves an intensity modulator. In fact, no light is transmitted when the retardation is 0, while all light is transmitted when the retardation is  $\pi$ . An acousto-optic modulator is a material that uses the piezoelectric and the photo-elastic effects to convert an oscillating electric field into mechanical vibrations, which in turn induce a spatially dependent index of refraction. When a standing acoustic wave is established, the acousto-optic crystal behaves as an oscillating refractive index grating that modulates the transmitted light by time-varying diffraction. Both electro-optic and acousto-optic devices require the light beam to be collimated. In the case of arc lamps, appropriate collimation optics are required. Pockels cells provide effective modulations up to about 500 MHz, and acousto-optic modulators up to about 300 MHz.

The wavelength of the laser is chosen on the basis of the requirements of the particular application (absorption band of a chromophore, optimal penetration depth in tissues, etc.). Examples of externally modulated CW lasers suitable for optical studies of tissues include the krypton ion (647 nm) and He-Ne (633 nm) lasers. Dye lasers pumped by either argon or krypton lasers afford continuous tunability over a wide spectral range that covers the whole visible band. Arc lamps (Xe, Xe-Hg, etc.) provide continuous spectral emission from the UV (230 nm) to the near-infrared (1100 nm). Therefore, they are ideal sources for spectroscopic studies when a wide and continuous spectral range is required.

### 7.2.2 Pulsed sources

It is possible to achieve a large modulation bandwidth by exploiting the harmonic content of pulsed sources with high repetition rates. These sources can be either mode-locked pulsed lasers (Nd:YAG, Ti:Sapphire, dye lasers, etc.)<sup>7</sup> or synchrotron radiation.<sup>8,9</sup> The repetition rate of the pulses gives the fundamental frequency, whereas the pulse width determines the width of the power spectrum band. The power spectrum of mode-locked lasers extends well above 10 GHz, an upper limit in frequency-domain spectroscopy imposed by the optical detectors rather than the light sources. The wavelengths of the above mentioned lasers are 1064 nm for the Nd:YAG, 660-1180 nm (tunable) for the Ti:Sapphire, and 625-780 nm (tunable) for dye lasers using DCM or oxanine 1 dyes. A

unique pulsed source is provided by synchrotron radiation, which continuously covers the UV/visible/near-infrared spectrum.

### 7.2.3 Laser diodes and light emitting diodes (LED's)

Semiconductor lasers and LED's can be intensity modulated by driving them with an oscillating current. As a result of the relatively fast response time of laser diodes, they can be modulated at frequencies up to the GHz range. The LED's modulation frequency bandwidth is typically limited to 150 MHz, and they emit light over a spectral bandwidth of about 50-80 nm. Consequently, LED's can be used to measure continuous spectra.<sup>10</sup> For frequency-domain tissue spectroscopy, one can find a number of laser diodes and LED's emitting in the wavelength region of interest extending from 600 to 1300 nm. Laser diodes are the most commonly used light sources in frequency-domain optical studies of tissue because of their cost-effectiveness, ease of modulation, and effective coupling to fiber optics, in addition to the fact that tissue spectroscopy can be effectively performed using a few discrete wavelengths (see sections 7.4.2 and 7.4.3).

### 7.2.4 Optical detectors

Optical detectors employed in frequency-domain spectroscopy include photomultiplier tubes (PMT's),<sup>11-14</sup> microchannel plate photomultipliers (MCP-PMT),<sup>15,16</sup> avalanche photodiodes (APD),<sup>17,18</sup> and charge coupled device (CCD) cameras in conjunction with a gated image intensifier.<sup>19,20</sup> In all cases, the down conversion from the source modulation frequency  $f$  to the cross-correlation frequency  $\Delta f$  (see section 7.2.5) can occur either internally to the detector, by modulating the detector gain at frequency  $f + \Delta f$ , or externally by electronically mixing the detector output at frequency  $f$  with the down conversion signal at frequency  $f + \Delta f$ . Photomultiplier tubes are very sensitive detectors. The cathode sensitivity is typically 50 mA/W, and a current amplification by about  $10^7$  determines an anode sensitivity as high as 1 A/ $\mu$ W. PMT's can operate in the visible and in the near-infrared up to about 1,000 nm. For internal down-conversion, their gain is modulated by a signal applied to the second dynode of the amplification chain. The typical rise time of a PMT, which is in the nanosecond range, allows for a modulation bandwidth of several hundred megahertz. The faster response of microchannel plates makes them suitable devices for modulation frequencies of up to several gigahertz. The frequency down-conversion can be performed by modulating the grid of the MCP-PMT<sup>15</sup> or by feeding the MCP-PMT output into an electronic mixer.<sup>16</sup> CCD cameras with modulated image intensifiers are powerful tools for frequency-domain spectroscopy, microscopy, and imaging. Finally, avalanche photodiodes can work at higher modulation frequencies and/or longer wavelengths than those

allowed by PMT's. The APD output is usually directed to an electronic mixer for frequency down-conversion.

### 7.2.5 Heterodyne detection, digital signal processing, and Fourier filtering

Heterodyne detection consists of down converting the frequency  $f$  of the detected signal to a lower frequency  $\Delta f$ . In the digital acquisition method,<sup>21</sup> after current-to-voltage conversion and low-pass filtering, the low frequency-signal is digitized. The A/D sampling rate is an integer multiple of  $\Delta f$  ( $n\Delta f$ ), so that the digital sampling is synchronous with the cross-correlation signal. The sampling theorem<sup>22</sup> states that  $n$  must be at least two for the complete determination of the harmonic at frequency  $\Delta f$ . A higher sampling rate allows for the discrimination of higher harmonics. Typical values of  $n$  range from 4 to 256. The digital signal processing consists of a preliminary average of the data sampled over a number of cross-correlation periods, followed by the discrimination of the frequency harmonic at  $\Delta f$  by discrete Fourier transform. The first filter (averaging) causes destructive interference of all the frequencies that are not multiples of  $\Delta f$ , while the discrete Fourier transform resolves each harmonic of  $\Delta f$ . The rejection of higher harmonics is accomplished by a factor greater than 2,000 (Ref. 21). Figure 7.1 shows a schematic illustration of the heterodyne detection and digital acquisition.

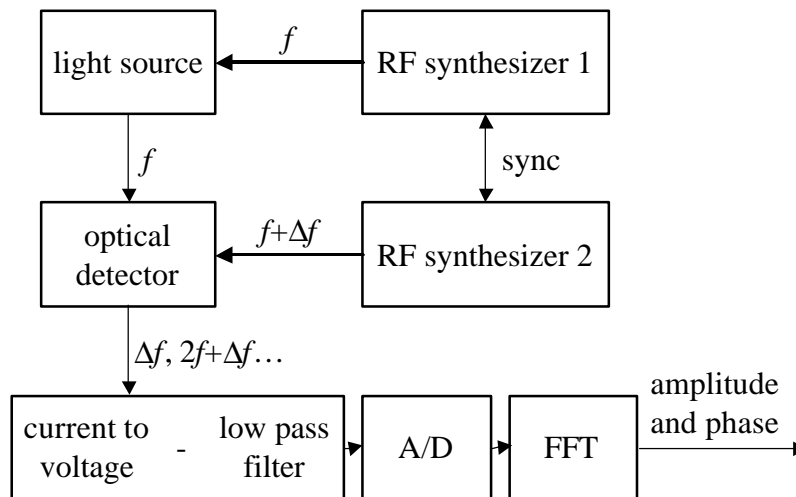


Fig. 7.1. Heterodyne detection scheme and digital signal processing with Fourier filter. The intensity of the light source is modulated at a radio-frequency (RF)  $f$ , typically on the order of 100 MHz. The beating between the detected signal at frequency  $f$  and the down-conversion signal at frequency  $f + \Delta f$  determines a low frequency component  $\Delta f$  that is filtered, digitized (A/D), and fast Fourier transformed (FFT) to yield the amplitude and phase readings. The two radio-frequency synthesizers are synchronized (sync).

## 7.2.6 A frequency-domain tissue spectrometer

We now describe a specific frequency-domain instrument for near-infrared spectroscopy and imaging of tissues. After the initial design and the implementation of a working prototype at the University of Illinois,<sup>23</sup> this instrument has undergone engineering and software development at ISS, Inc., Champaign, IL. A schematic diagram of the instrument is shown in Fig. 7.2. The light sources are laser diodes that are DC biased near threshold for laser operation. A superimposed 110 MHz radio-frequency current signal modulates the optical output of the laser diodes with a modulation depth close to 100%. The optical detectors are photomultiplier tubes (PMT's) (Hamamatsu Photonics R928) whose sensitivity is modulated by a 110.005 MHz signal (amplitude: ~32 dBm) applied to the second dynode. This heterodyne detection scheme down converts the 110 MHz signal to a frequency of 5 kHz, which is called the cross-correlation frequency. The signal processing proceeds as shown in Fig. 7.1 to yield the average value, the amplitude, and the phase of the detected modulated signal. The choice of the laser diodes for tissue oximetry (case shown in Fig. 7.2) is dictated by the requirement of having two wavelengths on the opposite sides of the isosbestic point at 800 nm for maximal sensitivity (see section 7.4.3). The choice of laser diodes emitting at 758 nm (Sharp LT030MD) and 830 nm (Sharp LT011MS) is ideal, as these wavelengths correspond to relatively flat portions of the absorption spectra of oxy-hemoglobin and deoxy-hemoglobin (see Fig. 7.4) (in particular, these wavelengths closely match a local maximum and a local minimum, respectively, in the deoxy-hemoglobin spectrum). However, the particular values of these wavelengths are not critical, so that the 758 nm lasers (now discontinued) can be replaced by 690 nm lasers (for instance, Hitachi HL6738MG). Furthermore, the laser diodes are mounted on interchangeable boards, so that one can change the laser wavelength according to the specific application. For instance, one can use boards containing lasers emitting at eight different wavelengths for tissue spectroscopy (for instance, Fig. 7.5 reports data collected at 633, 670, 751, 776, 786, 814, 830, and 841 nm [Ref. 24]). Alternatively, one can use a laser board containing diodes emitting at the same wavelength to maximize the number of source locations in single-wavelength optical imaging. In general, the instrument provides two parallel detectors and sixteen sources, resulting in thirty-two source-detector channels. The optical probes shown in Fig. 7.2 are designed to perform quantitative tissue oximetry. They implement the multi-distance measurement scheme<sup>10,25</sup> that was found to be robust and accurate for *in vivo* applications. This scheme consists of placing multiple (in this case, four) source fibers at different distances from the single detector fiber. In this fashion, one measures the spatial dependence of the DC intensity, AC amplitude, and phase data, which is related to the tissue optical coefficients by a diffusion model (see section 7.3.7). If two wavelengths are used, each illumination location consists of two source fibers (one per wavelength). One of the advantages of the multi-distance scheme is its insensitivity to motion artifacts, which allows for measurement

while the subject moves or exercises (see Fig. 7.6(c)). Multiple laser diodes time-share the optical detector by means of a multiplexing circuit that turns the laser diodes on and off in sequence, so that only one laser is on at any given time. The multiplexing rate, which determines the on-time of each laser diode, is adjustable by software. A typical multiplexing rate of 100 Hz corresponds to a 10-ms on-time per diode. The laser rise time, determined by protection circuitry, is about 1 ms. Therefore, the data collected during the first 1 ms of the on-time period of each laser are discarded. During a typical 10 ms long laser on-time, forty-five cross-correlation periods are processed (the 5 kHz cross-correlation frequency corresponds to a period of 0.2 ms). As few as twenty-five cross-correlation periods (5 ms) can be processed per laser on-time, leading to a maximum multiplexing rate of about 170 Hz. Faster computers and higher cross-correlation frequencies may further increase the data acquisition rate. A number of multiplexing cycles (selected by software) can be averaged to increase the signal-to-noise ratio when fast measurements are not required.

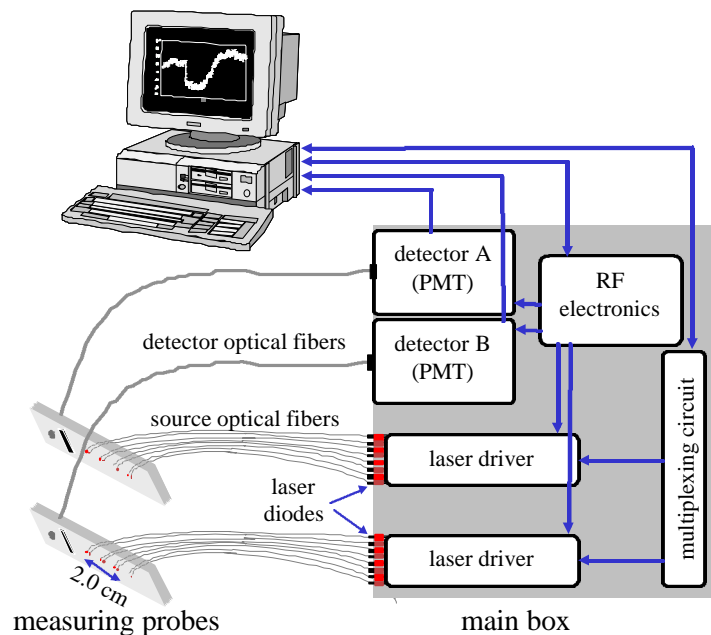


Fig. 7.2. Schematic diagram of a frequency-domain tissue spectrometer (Model 96208, ISS, Inc., Champaign, IL). In the configuration for tissue oximetry (shown here), each optical probe contains eight illuminating optical fibers and one detecting optical fiber. These fibers are coupled to eight laser diodes (four emitting at 690 nm and four at 830 nm) and to a photomultiplier tube (PMT) detector, respectively. RF electronics modulate the output of the light sources at a frequency of 110 MHz, and the PMT gain at a frequency of 110.005 MHz. A multiplexing circuit turns the lasers on and off in sequence at an adjustable rate controlled by the software (a typical multiplexing rate of 100 Hz corresponds to a 10-ms on-time per laser). The two optical probes can operate in parallel at two different tissue locations.

The instrumental noise, which depends on the acquisition time, is typically much smaller than the physiological fluctuations observed *in vivo*. The noise can be estimated by the standard deviation of the temporal fluctuations of the measured data. Figure 7.3 shows typical temporal traces of the average intensity, amplitude, phase, absorption coefficient, and reduced scattering coefficient measured with an acquisition time per diode of 160 ms (average of sixteen 10-ms cycles) on a tissue-like solid phantom (made of silicone). The optical coefficients of the phantom (Fig. 7.3(d)) match typical optical properties of blood-perfused tissues in the near-infrared. The standard deviation errors in the various readings are reported in Table 7.1. The instrumental errors decrease for longer acquisition times.

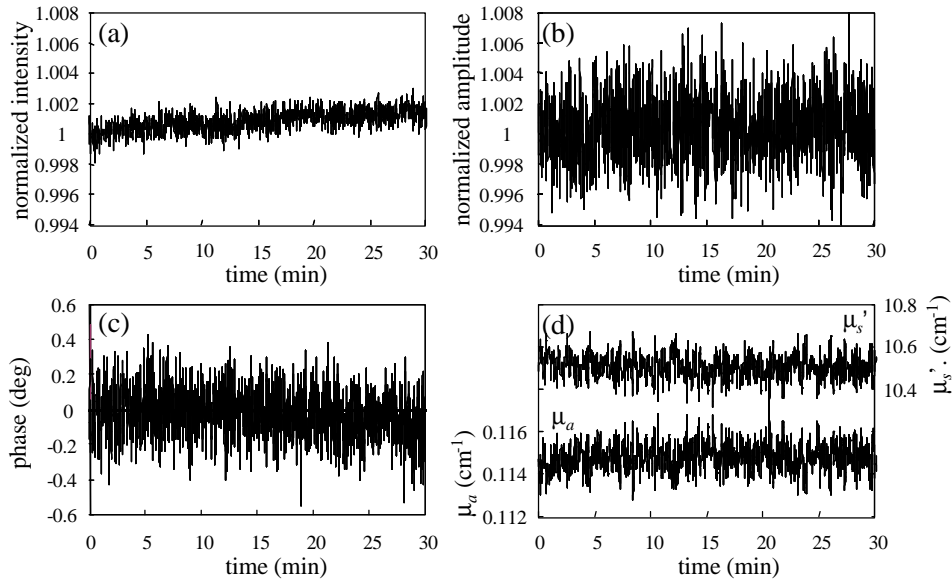


Fig. 7.3. Temporal traces of the (a) normalized average intensity, (b) normalized amplitude, (c) phase, and (d) absorption ( $\mu_a$ ) and reduced scattering ( $\mu_s'$ ) coefficients measured at 690 nm on a synthetic tissue-like phantom with the instrument of Fig. 7.2. The acquisition time for the average intensity, the amplitude, and the phase is 160 ms (10 ms on-time per laser diode, sixteen multiplexing cycles averaged), and the source-detector separation is 2.5 cm. The four-distance measurement scheme of the absorption and reduced scattering coefficients (range of source-detector separations: 2.0-3.5 cm) determines an acquisition time of 640 ms (160 ms/diode  $\times$  4 diodes) for the optical coefficients.

Table 7.1. Instrumental noise estimated by the temporal standard deviation of the raw data (average intensity, amplitude, and phase) and the optical coefficients (absorption and reduced scattering) measured on a solid tissue-like phantom with the frequency-domain tissue spectrometer of Fig. 7.2. The acquisition time for the raw data (average intensity, amplitude, and phase) is 160 ms. Because the measurement of the optical coefficients at each wavelength requires the readings from four source locations (four source-detector separations), the acquisition time for  $\mu_a$  and  $\mu_s'$  is  $160 \text{ ms} \times 4 = 640 \text{ ms}$ .

Parameter	Acquisition time (ms)	Instrumental noise	
		@ 690 nm	@ 830 nm
Average Intensity (DC)	160	0.05%	0.05%
Amplitude (AC)	160	0.2%	0.1%
Phase ( $\Phi$ )	160	0.1°	0.1°
Absorption coefficient ( $\mu_a$ )	640	0.0007 $\text{cm}^{-1}$	0.0006 $\text{cm}^{-1}$
Reduced scattering coefficient ( $\mu_s'$ )	640	0.05 $\text{cm}^{-1}$	0.04 $\text{cm}^{-1}$

### 7.3 Modeling light propagation in scattering media

#### 7.3.1 The Boltzmann transport equation (BTE)

The Boltzmann transport equation (BTE) is a balance relationship that describes the flow of particles in scattering and absorbing media. The propagation of light in optically turbid media can be modeled by the transport equation, where the photons are treated as the transported particles. If we denote the angular photon density with  $u(\mathbf{r}, \hat{\Omega}, t)$ , which is defined as the number of photons per unit volume per unit solid angle traveling in direction  $\hat{\Omega}$  at position  $\mathbf{r}$  and time  $t$ , we can write the BTE as follows:<sup>26</sup>

$$\begin{aligned} \frac{\partial u(\mathbf{r}, \hat{\Omega}, t)}{\partial t} = & -v\hat{\Omega} \cdot \nabla u(\mathbf{r}, \hat{\Omega}, t) - v(\mu_a + \mu_s)u(\mathbf{r}, \hat{\Omega}, t) \\ & + v\mu_s \int_{4\pi} u(\mathbf{r}, \hat{\Omega}', t) f(\hat{\Omega}', \hat{\Omega}) d\hat{\Omega}' + q(\mathbf{r}, \hat{\Omega}, t), \end{aligned} \quad (7.1)$$

where  $v$  is the speed of light in the medium,  $\mu_a$  is the absorption coefficient (units of  $\text{cm}^{-1}$ ),  $\mu_s$  is the scattering coefficient (units of  $\text{cm}^{-1}$ ),  $f(\hat{\Omega}', \hat{\Omega})$  is the phase function or the probability density of scattering a photon that travels along direction  $\hat{\Omega}'$  into direction  $\hat{\Omega}$ , and  $q(\mathbf{r}, \hat{\Omega}, t)$  is the source term.  $q(\mathbf{r}, \hat{\Omega}, t)$  has units of  $\text{s}^{-1}\text{m}^{-3}\text{sr}^{-1}$  and represents the number of photons injected by the light source per unit volume, per unit time, per unit solid angle at position  $\mathbf{r}$ , time  $t$ , and direction  $\hat{\Omega}$ . The left hand side of Eq. (7.1) represents the temporal variation of the angular photon density. Each one of the terms on the right hand side represents a specific contribution to this variation. The first term is the net

gain of photons at position  $\mathbf{r}$  and direction  $\hat{\Omega}$  due to the flow of photons. The second term is the loss of photons at  $\mathbf{r}$  and  $\hat{\Omega}$  as a result of collisions (absorption and scattering). The third term is the gain of photons at  $\mathbf{r}$  and  $\hat{\Omega}$  due to scattering. Finally, the fourth term is the gain of photons due to the light sources. Let us now define some of the quantities used to describe photon transport.

Angular photon density:  $u(\mathbf{r}, \hat{\Omega}, t)$

$u(\mathbf{r}, \hat{\Omega}, t)$  is defined such that  $u(\mathbf{r}, \hat{\Omega}, t)d\mathbf{r}d\hat{\Omega}$  represents the number of photons in  $d\mathbf{r}$  that travel in a direction within  $d\hat{\Omega}$  around  $\hat{\Omega}$ . The units of  $u(\mathbf{r}, \hat{\Omega}, t)$  are  $\text{m}^{-3}\text{sr}^{-1}$ .

Photon radiance:  $L(\mathbf{r}, \hat{\Omega}, t)$

$L(\mathbf{r}, \hat{\Omega}, t) = \nu u(\mathbf{r}, \hat{\Omega}, t)$ .  $L(\mathbf{r}, \hat{\Omega}, t)d\hat{\Omega}$  represents the number of photons traveling per unit time per unit area (perpendicular to  $\hat{\Omega}$ ) in a range of directions within  $d\hat{\Omega}$  around  $\hat{\Omega}$ . The units of  $L(\mathbf{r}, \hat{\Omega}, t)$  are  $\text{s}^{-1}\text{m}^{-2}\text{sr}^{-1}$ .

Photon density:  $U(\mathbf{r}, t)$

$U(\mathbf{r}, t) = \int_{4\pi} u(\mathbf{r}, \hat{\Omega}, t)d\hat{\Omega}$ . The photon density is the number of photons per unit volume. The units are  $\text{m}^{-3}$ .

Photon fluence rate:  $E_0(\mathbf{r}, t)$

$E_0(\mathbf{r}, t) = \nu U(\mathbf{r}, t) = \int_{4\pi} L(\mathbf{r}, \hat{\Omega}, t)d\hat{\Omega}$ . The photon fluence rate is defined as the number of photons traveling per unit time per unit area (perpendicular to the direction of propagation) over all directions. The units are  $\text{s}^{-1}\text{m}^{-2}$ .

Photon current density, or photon flux:  $\mathbf{J}(\mathbf{r}, t)$

$\mathbf{J}(\mathbf{r}, t) = \int_{4\pi} L(\mathbf{r}, \hat{\Omega}, t)\hat{\Omega}d\hat{\Omega}$ . The photon flux is a vector that represents the net flow of photons. Its direction points in the direction of the net flux, while its amplitude gives the net number of photons transmitted per unit time per unit area in that direction. The units of  $\mathbf{J}(\mathbf{r}, t)$  are  $\text{s}^{-1}\text{m}^{-2}$ .

The above definitions can be extended to describe radiant energy (instead of photon number) by replacing the word “photon” with “energy,” and by introducing a factor  $h\nu$  in all definitions ( $h\nu$  is the energy per photon, where  $h$  is Planck’s constant and  $\nu$  is the light frequency). A complete nomenclature for quantities used in medical optics can be found in Ref. 27.

### 7.3.2 Expansion of the Boltzmann equation in spherical harmonics

To model light propagation in highly scattering media, as are most biological tissues, it is useful to expand the angular photon density  $u(\mathbf{r}, \hat{\Omega}, t)$ , the source term  $q(\mathbf{r}, \hat{\Omega}, t)$ , and the phase function  $f(\hat{\Omega}', \hat{\Omega})$  into spherical harmonics  $Y_l^m(\hat{\Omega})$ .<sup>28-30</sup> The so-called  $P_N$  approximation to the Boltzmann equation (see Section 7.3.3) is based on such an expansion. As a result of the completeness property of the spherical harmonics, any function  $h(\theta, \varphi)$  (with sufficient continuity properties) can be expanded in the Laplace series:<sup>31</sup>

$$h(\theta, \varphi) = \sum_{l=0}^{\infty} \sum_{m=-l}^l h_{lm} Y_l^m(\hat{\Omega}), \quad (7.2)$$

where  $h_{lm}$  are coefficients independent of  $\theta$  and  $\varphi$ , and the relationship among  $\theta$ ,  $\varphi$ , and  $\hat{\Omega}$  is  $\hat{\Omega} = \sin \theta \cos \varphi \hat{\mathbf{x}} + \sin \theta \sin \varphi \hat{\mathbf{y}} + \cos \theta \hat{\mathbf{z}}$ . Accordingly, we expand  $u(\mathbf{r}, \hat{\Omega}, t)$  and  $q(\mathbf{r}, \hat{\Omega}, t)$  into spherical harmonics as follows:

$$u(\mathbf{r}, \hat{\Omega}, t) = \sum_{l=0}^{\infty} \sum_{m=-l}^l u_{lm}(\mathbf{r}, t) Y_l^m(\hat{\Omega}), \quad (7.3)$$

$$q(\mathbf{r}, \hat{\Omega}, t) = \sum_{l=0}^{\infty} \sum_{m=-l}^l q_{lm}(\mathbf{r}, t) Y_l^m(\hat{\Omega}). \quad (7.4)$$

We assume that the phase function  $f(\hat{\Omega}', \hat{\Omega})$  only depends on  $\hat{\Omega}' \cdot \hat{\Omega}$  (i.e. on the cosine of the scattering angle  $\gamma$ ). We can thus expand  $f(\hat{\Omega}', \hat{\Omega})$  in Legendre polynomials, by recalling that a function  $H(x)$  (which is sectionally continuous together with its derivative in the interval  $[-1, 1]$ ) has the general Legendre series representation:<sup>31</sup>

$$H(x) = \sum_{l=0}^{\infty} \frac{2l+1}{2} H_l P_l(x). \quad (7.5)$$

where  $P_l(x)$  is the Legendre polynomial of order  $l$ , and  $H_l = \int_{-1}^1 H(x') P_l(x') dx'$ . We then write:

$$\begin{aligned} f(\hat{\Omega}' \cdot \hat{\Omega}) &= \sum_{l=0}^{\infty} \frac{2l+1}{4\pi} f_l P_l(\hat{\Omega}' \cdot \hat{\Omega}) \\ &= \sum_{l=0}^{\infty} \sum_{m=-l}^l f_l Y_l^{m*}(\hat{\Omega}') Y_l^m(\hat{\Omega}), \end{aligned} \quad (7.6)$$

where the last expression follows from the addition theorem for spherical harmonics,<sup>31</sup> namely  $P_l(\hat{\Omega}' \cdot \hat{\Omega}) = 4\pi/(2l+1) \sum_{m=-l}^l Y_l^{m*}(\hat{\Omega}') Y_l^m(\hat{\Omega})$ . Here,

$$f_l = 2\pi \int_{-1}^1 f(\cos \gamma) P_l(\cos \gamma) d(\cos \gamma).$$

By substituting these expressions into Eq. (7.1), we obtain:

$$\begin{aligned} \sum_{l=0}^{\infty} \sum_{m=-l}^l \left\{ \left[ \frac{\partial}{\partial t} + v\hat{\Omega} \cdot \nabla + v(\mu_a + \mu_s) \right] u_{lm}(\mathbf{r}, t) Y_l^m(\hat{\Omega}) - q_{lm}(\mathbf{r}, t) Y_l^m(\hat{\Omega}) \right. \\ \left. - v\mu_s \int_{4\pi} u_{lm}(\mathbf{r}, t) Y_l^m(\hat{\Omega}') \sum_{l'=0}^{\infty} \sum_{m'=-l'}^{l'} f_{l'} Y_{l'}^{m'*}(\hat{\Omega}') Y_{l'}^{m'}(\hat{\Omega}) d\hat{\Omega}' \right\} = 0. \quad (7.7) \end{aligned}$$

The integral in  $d\hat{\Omega}'$  can be calculated using the orthogonality property of the spherical harmonics:  $\int_{4\pi} Y_l^{m*}(\hat{\Omega}) Y_{l'}^{m'}(\hat{\Omega}) d\hat{\Omega} = \delta_{ll'} \delta_{mm'}$ . The BTE thus becomes:

$$\sum_{l=0}^{\infty} \sum_{m=-l}^l \left\{ \left[ \frac{\partial}{\partial t} + v\hat{\Omega} \cdot \nabla + v[\mu_s(1-f_l) + \mu_a] \right] u_{lm}(\mathbf{r}, t) - q_{lm}(\mathbf{r}, t) \right\} Y_l^m(\hat{\Omega}) = 0. \quad (7.8)$$

We then multiply this equation by  $Y_L^{M*}(\hat{\Omega})$  and integrate over  $\hat{\Omega}$  to obtain the relationship between the specific coefficients  $u_{LM}$  and  $q_{LM}$ , and all the coefficients of the spherical harmonic expansion of  $u$ ,  $u_{lm}$ :

$$\begin{aligned} \frac{\partial}{\partial t} u_{LM}(\mathbf{r}, t) + v[\mu_s(1-f_l) + \mu_a] u_{LM}(\mathbf{r}, t) \\ + v \sum_{l=0}^{\infty} \sum_{m=-l}^l \int_{4\pi} \hat{\Omega} \cdot \nabla u_{lm}(\mathbf{r}, t) Y_l^m(\hat{\Omega}) Y_L^{M*}(\hat{\Omega}) d\hat{\Omega} = q_{LM}(\mathbf{r}, t). \quad (7.9) \end{aligned}$$

The integral over  $\hat{\Omega}$  can be evaluated by writing the  $x$ ,  $y$ , and  $z$  components of the vector  $Y_L^M(\hat{\Omega})\hat{\Omega}$  in terms of spherical harmonics. This can be done by using the recurrence relations for the associated Legendre functions  $P_l^m(x)$ . The result is the following:

$$\begin{aligned}
Y_L^M(\hat{\Omega})\Omega_x &= Y_L^M(\hat{\Omega})\sin\theta\cos\varphi \\
&= -\frac{1}{2}\left[\frac{(L+M+1)(L+M+2)}{(2L+1)(2L+3)}\right]^{1/2} Y_{L+1}^{M+1}(\hat{\Omega}) \\
&\quad + \frac{1}{2}\left[\frac{(L-M)(L-M-1)}{(2L-1)(2L+1)}\right]^{1/2} Y_{L-1}^{M+1}(\hat{\Omega}) \\
&\quad + \frac{1}{2}\left[\frac{(L-M+1)(L-M+2)}{(2L+1)(2L+3)}\right]^{1/2} Y_{L+1}^{M-1}(\hat{\Omega}) \\
&\quad - \frac{1}{2}\left[\frac{(L+M)(L+M-1)}{(2L-1)(2L+1)}\right]^{1/2} Y_{L-1}^{M-1}(\hat{\Omega}),
\end{aligned} \tag{7.10}$$

$$\begin{aligned}
Y_L^M(\hat{\Omega})\Omega_y &= Y_L^M(\hat{\Omega})\sin\theta\sin\varphi \\
&= -\frac{1}{2i}\left[\frac{(L+M+1)(L+M+2)}{(2L+1)(2L+3)}\right]^{1/2} Y_{L+1}^{M+1}(\hat{\Omega}) \\
&\quad + \frac{1}{2i}\left[\frac{(L-M)(L-M-1)}{(2L-1)(2L+1)}\right]^{1/2} Y_{L-1}^{M+1}(\hat{\Omega}) \\
&\quad - \frac{1}{2i}\left[\frac{(L-M+1)(L-M+2)}{(2L+1)(2L+3)}\right]^{1/2} Y_{L+1}^{M-1}(\hat{\Omega}) \\
&\quad + \frac{1}{2i}\left[\frac{(L+M)(L+M-1)}{(2L-1)(2L+1)}\right]^{1/2} Y_{L-1}^{M-1}(\hat{\Omega}),
\end{aligned} \tag{7.11}$$

$$\begin{aligned}
Y_L^M(\hat{\Omega})\Omega_z &= Y_L^M(\hat{\Omega})\cos\theta \\
&= \left[\frac{(L-M+1)(L+M+1)}{(2L+1)(2L+3)}\right]^{1/2} Y_{L+1}^M(\hat{\Omega}) \\
&\quad + \left[\frac{(L-M)(L+M)}{(2L-1)(2L+1)}\right]^{1/2} Y_{L-1}^M(\hat{\Omega}).
\end{aligned} \tag{7.12}$$

Using these expressions for the  $x$ ,  $y$ , and  $z$  components of  $Y_L^M(\hat{\Omega})\hat{\Omega}$ , it is possible to calculate the integral using the orthogonality relations for spherical harmonics. We find that the relationship between the specific coefficients  $u_{LM}$  and  $q_{LM}$  does not involve all the coefficients of the spherical harmonic expansion of  $u$ ,  $u_{lm}$ , but it only contains  $u_{lm}$  with indices  $l$  ranging from  $L-1$  to  $L+1$ , and  $m$  ranging from  $M-1$  to  $M+1$ :

$$\begin{aligned}
& \frac{\partial}{\partial t} u_{LM}(\mathbf{r}, t) + v[\mu_s(1-f_L) + \mu_a] u_{LM}(\mathbf{r}, t) \\
& + \frac{1}{2} \left[ \frac{(L-M+1)(L-M+2)}{(2L+1)(2L+3)} \right]^{1/2} \left( \frac{\partial}{\partial x} - i \frac{\partial}{\partial y} \right) v u_{L+1}^{M-1}(\mathbf{r}, t) \\
& - \frac{1}{2} \left[ \frac{(L+M)(L+M-1)}{(2L+1)(2L-1)} \right]^{1/2} \left( \frac{\partial}{\partial x} - i \frac{\partial}{\partial y} \right) v u_{L-1}^{M-1}(\mathbf{r}, t) \\
& - \frac{1}{2} \left[ \frac{(L+M+2)(L+M+1)}{(2L+1)(2L+3)} \right]^{1/2} \left( \frac{\partial}{\partial x} + i \frac{\partial}{\partial y} \right) v u_{L+1}^{M+1}(\mathbf{r}, t) \\
& + \frac{1}{2} \left[ \frac{(L-M-1)(L-M)}{(2L+1)(2L-1)} \right]^{1/2} \left( \frac{\partial}{\partial x} + i \frac{\partial}{\partial y} \right) v u_{L-1}^{M+1}(\mathbf{r}, t) \\
& + \left[ \frac{(L+M+1)(L-M+1)}{(2L+1)(2L+3)} \right]^{1/2} \frac{\partial}{\partial z} v u_{L+1}^M(\mathbf{r}, t) \\
& + \left[ \frac{(L-M)(L+M)}{(2L-1)(2L+1)} \right]^{1/2} \frac{\partial}{\partial z} v u_{L-1}^M(\mathbf{r}, t) = q_{LM}(\mathbf{r}, t). \tag{7.13}
\end{aligned}$$

### 7.3.3 The $P_N$ approximation

The expansion of the BTE into spherical harmonics has led to an infinite set of equations with indices  $L$  (ranging from 0 to  $\infty$ ) and  $M$  (ranging from  $-L$  to  $L$ ). Truncation of the Laplace series at  $L = N$ , leads to the so-called  $P_N$  approximation. The reason for this name is that the last term in the truncated Laplace series contains  $Y_N^M(\hat{\Omega})$  which can be written in terms of the associated Legendre functions  $P_N^M(x)$ , which in turn can be written in terms of the Legendre polynomial  $P_N(x)$ . The relationships are the following:

$$Y_N^M(\hat{\Omega}) = (-1)^M \left[ \frac{(2N+1)(N-M)!}{4\pi(N+M)!} \right]^{1/2} P_N^M(\cos \theta) e^{iM\phi}, \tag{7.14}$$

$$P_N^M(x) = (1-x^2)^{M/2} \frac{d^M}{dx^M} P_N(x). \tag{7.15}$$

### 7.3.4 The $P_1$ approximation

We now consider the  $P_1$  approximation, which is often used to describe photon migration in tissues. In the  $P_1$  approximation  $u_{LM}(\mathbf{r}, t)$  is set to 0 for  $L > 1$ . In the  $P_1$  approximation, Eq. (7.13) is a set of 4 equations. The first, for  $L=0, M=0$ :

$$\begin{aligned} & \frac{\partial}{\partial t} u_{0,0}(\mathbf{r}, t) + v[\mu_s(1 - f_0) + \mu_a] u_{0,0}(\mathbf{r}, t) \\ & + \frac{1}{2} \sqrt{\frac{2}{3}} \left( \frac{\partial}{\partial x} - i \frac{\partial}{\partial y} \right) v u_{1,-1}(\mathbf{r}, t) \\ & - \frac{1}{2} \sqrt{\frac{2}{3}} \left( \frac{\partial}{\partial x} + i \frac{\partial}{\partial y} \right) v u_{1,1}(\mathbf{r}, t) + \sqrt{\frac{1}{3}} \frac{\partial}{\partial z} v u_{1,0}(\mathbf{r}, t) = q_{0,0}(\mathbf{r}, t), \end{aligned} \quad (7.16)$$

the second, for  $L=1, M=-1$ :

$$\begin{aligned} & \frac{\partial}{\partial t} u_{1,-1}(\mathbf{r}, t) + v[\mu_s(1 - f_1) + \mu_a] u_{1,-1}(\mathbf{r}, t) \\ & + \frac{1}{2} \sqrt{\frac{2}{3}} \left( \frac{\partial}{\partial x} + i \frac{\partial}{\partial y} \right) v u_{0,0}(\mathbf{r}, t) = q_{1,-1}(\mathbf{r}, t), \end{aligned} \quad (7.17)$$

the third, for  $L=1, M=0$ :

$$\begin{aligned} & \frac{\partial}{\partial t} u_{1,0}(\mathbf{r}, t) + v[\mu_s(1 - f_1) + \mu_a] u_{1,0}(\mathbf{r}, t) \\ & + \sqrt{\frac{1}{3}} \frac{\partial}{\partial z} v u_{0,0}(\mathbf{r}, t) = q_{1,0}(\mathbf{r}, t), \end{aligned} \quad (7.18)$$

and the fourth, for  $L=1, M=1$ :

$$\begin{aligned} & \frac{\partial}{\partial t} u_{1,1}(\mathbf{r}, t) + v[\mu_s(1 - f_1) + \mu_a] u_{1,1}(\mathbf{r}, t) \\ & - \frac{1}{2} \sqrt{\frac{2}{3}} \left( \frac{\partial}{\partial x} - i \frac{\partial}{\partial y} \right) v u_{0,0}(\mathbf{r}, t) = q_{1,1}(\mathbf{r}, t). \end{aligned} \quad (7.19)$$

The coefficients  $u_{0,0}(\mathbf{r}, t)$  and  $u_{1,M}(\mathbf{r}, t)$  are related to the photon density  $U(\mathbf{r}, t)$  and to the photon flux  $\mathbf{J}(\mathbf{r}, t)$ , respectively. In fact:

$$\begin{aligned} U(\mathbf{r}, t) &= \int_{4\pi} u(\mathbf{r}, \hat{\Omega}, t) d\hat{\Omega} \\ &= \sum_{l=0}^{\infty} \sum_{m=-l}^l u_{lm}(\mathbf{r}, t) \int_{4\pi} Y_l^m(\hat{\Omega}) d\hat{\Omega} = \sqrt{4\pi} u_{0,0}(\mathbf{r}, t), \end{aligned} \quad (7.20)$$

(since  $\int_{4\pi} Y_l^m(\hat{\Omega}) d\hat{\Omega} = 0$  for  $m \neq 0$  and  $Y_0^0(\hat{\Omega}) = 1/\sqrt{4\pi}$ ), and:

$$\begin{aligned}
\mathbf{J}(\mathbf{r}, t) &= \int_{4\pi} v u(\mathbf{r}, \hat{\Omega}, t) \hat{\Omega} d\hat{\Omega} \\
&= \sum_{l=0}^{\infty} \sum_{m=-l}^l v u_{lm}(\mathbf{r}, t) \int_{4\pi} (\sin \theta \cos \varphi \hat{\mathbf{x}} + \sin \theta \sin \varphi \hat{\mathbf{y}} + \cos \theta \hat{\mathbf{z}}) Y_l^m(\hat{\Omega}) d\hat{\Omega} \\
&= \sum_{l=0}^{\infty} \sum_{m=-l}^l v u_{lm}(\mathbf{r}, t) \int_{4\pi} \sqrt{\frac{4\pi}{3}} \left\{ \begin{aligned} &\sqrt{\frac{1}{2}} [-Y_1^{1*}(\hat{\Omega}) + Y_1^{-1*}(\hat{\Omega})] \hat{\mathbf{x}} \\ &+ \sqrt{\frac{1}{2}} \frac{1}{i} [Y_1^{1*}(\hat{\Omega}) + Y_1^{-1*}(\hat{\Omega})] \hat{\mathbf{y}} + Y_1^0(\hat{\Omega}) \hat{\mathbf{z}} \end{aligned} \right\} Y_l^m(\hat{\Omega}) d\hat{\Omega} \\
&= \sqrt{\frac{4\pi}{3}} v \left[ \sqrt{\frac{1}{2}} (-u_{1,1}(\mathbf{r}, t) + u_{1,-1}(\mathbf{r}, t)) \hat{\mathbf{x}} - i \sqrt{\frac{1}{2}} (u_{1,1}(\mathbf{r}, t) + u_{1,-1}(\mathbf{r}, t)) \hat{\mathbf{y}} + u_{1,0}(\mathbf{r}, t) \hat{\mathbf{z}} \right].
\end{aligned} \tag{7.21}$$

The set of four equations (7.16)-(7.19) of the  $P_1$  approximation are thus equivalent to the following two equations (one scalar and one vectorial):

$$\frac{\partial}{\partial t} U(\mathbf{r}, t) + v [\mu_s (1 - f_0) + \mu_a] U(\mathbf{r}, t) + \nabla \cdot \mathbf{J}(\mathbf{r}, t) = \sqrt{4\pi} q_{0,0}(\mathbf{r}, t), \tag{7.22}$$

$$\begin{aligned}
\frac{1}{v} \frac{\partial}{\partial t} \mathbf{J}(\mathbf{r}, t) + [\mu_s (1 - f_1) + \mu_a] \mathbf{J}(\mathbf{r}, t) + \frac{1}{3} v \nabla U(\mathbf{r}, t) &= \\
= \sqrt{\frac{4\pi}{3}} \left[ \sqrt{\frac{1}{2}} (q_{1,-1}(\mathbf{r}, t) - q_{1,1}(\mathbf{r}, t)) \hat{\mathbf{x}} - i \sqrt{\frac{1}{2}} (q_{1,-1}(\mathbf{r}, t) + q_{1,1}(\mathbf{r}, t)) \hat{\mathbf{y}} + q_{1,0}(\mathbf{r}, t) \hat{\mathbf{z}} \right].
\end{aligned} \tag{7.23}$$

The vectorial equation is obtained by combining Eqs. (7.17), (7.18), (7.19) according to the following formal relationship:

$\sqrt{2\pi/3}[(7.17) - (7.19)] \hat{\mathbf{x}} - i \sqrt{2\pi/3}[(7.17) + (7.19)] \hat{\mathbf{y}} + \sqrt{4\pi/3}(7.18) \hat{\mathbf{z}}$ . From the general definition of the coefficients  $f_l$ , we find that  $f_0$  and  $f_1$  are given by:

$$f_0 = 2\pi \int_{-1}^1 f(\cos \gamma) P_0(\cos \gamma) d(\cos \gamma) = 2\pi \int_{-1}^1 f(\cos \gamma) d(\cos \gamma) = 1, \tag{7.24}$$

$$f_1 = 2\pi \int_{-1}^1 f(\cos \gamma) P_1(\cos \gamma) d(\cos \gamma) = 2\pi \int_{-1}^1 f(\cos \gamma) \cos \gamma d(\cos \gamma) = \langle \cos \gamma \rangle, \tag{7.25}$$

where in Eq. (7.24) we have used the fact that the scattering probability is normalized according to the condition  $\int_{4\pi} f(\hat{\Omega}' \cdot \hat{\Omega}) d\hat{\Omega}' = 1$ , which is equivalent to  $2\pi \int_{-1}^1 f(\cos \gamma) d(\cos \gamma) = 1$ . Therefore  $f_0$  is 1, whereas  $f_1$  is the average cosine of the scattering angle  $\gamma$  ( $\langle \cos \gamma \rangle$ ). The source terms in Eqs. (7.22) and (7.23) are formally a monopole term (spherically symmetric) and a dipole term,

respectively. We will indicate them with the symbols  $S_0(\mathbf{r},t)$  and  $\mathbf{S}_1(\mathbf{r},t)$ , respectively. The final expressions for the  $P_1$  equations are:

$$\frac{\partial}{\partial t}U(\mathbf{r},t) + v\mu_a U(\mathbf{r},t) + \nabla \cdot \mathbf{J}(\mathbf{r},t) = S_0(\mathbf{r},t), \quad (7.26)$$

$$\frac{1}{v} \frac{\partial}{\partial t} \mathbf{J}(\mathbf{r},t) + [\mu_s(1 - \langle \cos \gamma \rangle) + \mu_a] \mathbf{J}(\mathbf{r},t) + \frac{1}{3} v \nabla U(\mathbf{r},t) = \mathbf{S}_1(\mathbf{r},t). \quad (7.27)$$

### 7.3.5 The reduced scattering coefficient

Equations (7.26) and (7.27) show that, in the  $P_1$  approximation,  $\mu_s$  and  $\cos \gamma$  only appear in the term  $\mu_s(1 - \langle \cos \gamma \rangle)$ . In this section, we give a physical meaning to this term on the basis of an analysis reported by Zaccanti *et al.*<sup>32</sup> Suppose that a photon is emitted at the point  $P_0 \equiv (0,0,0)$  in direction  $\hat{\mathbf{z}}$ . This photon will first be scattered at a point  $P_1 \equiv (x_1, y_1, z_1)$  after having traveled a distance  $r_1$ . Then it will be scattered at point  $P_2 \equiv (x_2, y_2, z_2)$  after having traveled a distance  $r_2$ , and so on. In general, we refer to the scattering at point  $P_n$  as the  $n$ -th order scattering. We want to define the reduced scattering coefficient,  $\mu'_s$ , as the inverse of the average distance projected along the  $z$  axis that the photon has to travel to lose memory of the initial direction of propagation. In other words,  $1/\mu'_s$  represents the average distance between what are effectively isotropic scattering events. In the derivation of  $\mu'_s$ , we neglect the absorption of the medium, since we are only interested in its scattering properties. The probability density,  $g(r)$ , of traveling a distance  $r$  without suffering a scattering event is defined as  $g(r) = \mu_s e^{-\mu_s r}$ . The first order scattering occurs at  $P_1 \equiv (0,0,r_1)$ , whose average coordinates are:<sup>32</sup>

$$\begin{aligned} \langle x_1 \rangle = \langle y_1 \rangle &= 0, \\ \langle z_1 \rangle &= \int_0^\infty r_1 g(r_1) dr_1 = \frac{1}{\mu_s}. \end{aligned} \quad (7.28)$$

The second order scattering occurs at  $P_2 \equiv (r_2 \sin \theta_2 \cos \varphi_2, r_2 \sin \theta_2 \sin \varphi_2, z_1 + r_2 \cos \theta_2)$ . Since  $r_1$ ,  $r_2$ ,  $\theta_2$ ,  $\varphi_2$  are not statistically correlated, the average values of the coordinates of  $P_2$  are:<sup>32</sup>

$$\begin{aligned} \langle x_2 \rangle &= \langle r_2 \rangle \langle \sin \theta_2 \rangle \langle \cos \varphi_2 \rangle = 0, \\ \langle y_2 \rangle &= \langle r_2 \rangle \langle \sin \theta_2 \rangle \langle \sin \varphi_2 \rangle = 0, \\ \langle z_2 \rangle &= \langle r_1 \rangle + \langle r_2 \rangle \langle \cos \theta_2 \rangle = \frac{1}{\mu_s} (1 + \langle \cos \gamma \rangle). \end{aligned} \quad (7.29)$$

The third order scattering occurs at  $P_3 \equiv (x_3, y_3, z_3)$  where:

$$\begin{aligned} x_3 &= x_2 + r_3 (\sin \theta_3 \cos \varphi_3 \cos \theta_2 \cos \varphi_2 - \sin \theta_3 \sin \varphi_3 \sin \varphi_2 + \cos \theta_3 \sin \theta_2 \cos \varphi_2), \\ y_3 &= y_2 + r_3 (\sin \theta_3 \cos \varphi_3 \cos \theta_2 \sin \varphi_2 + \sin \theta_3 \sin \varphi_3 \cos \varphi_2 + \cos \theta_3 \sin \theta_2 \sin \varphi_2), \\ z_3 &= z_2 + r_3 (-\sin \theta_3 \cos \varphi_3 \sin \theta_2 + \cos \theta_3 \cos \theta_2). \end{aligned} \quad (7.30)$$

The average values of the coordinates of  $P_3$  are:<sup>32</sup>

$$\begin{aligned} \langle x_3 \rangle &= \langle y_3 \rangle = 0, \\ \langle z_3 \rangle &= \frac{1}{\mu_s} (1 + \langle \cos \theta \rangle + \langle \cos \theta \rangle^2). \end{aligned} \quad (7.31)$$

In general, at the  $n$ -th order of scattering, the average values of the coordinates of the scattering point  $P_n$  are:<sup>32</sup>

$$\begin{aligned} \langle x_n \rangle &= \langle y_n \rangle = 0, \\ \langle z_n \rangle &= \frac{1}{\mu_s} \sum_{k=0}^{n-1} \langle \cos \gamma \rangle^k = \frac{1 - \langle \cos \gamma \rangle^n}{\mu_s (1 - \langle \cos \gamma \rangle)}, \end{aligned} \quad (7.32)$$

where we have used the result for the geometric series  $\sum_{k=0}^{n-1} a^k = \frac{1-a^n}{1-a}$ , with  $a < 1$ . In the limit of a high number of scattering events ( $n \rightarrow \infty$ ),  $\langle x_\infty \rangle = \langle y_\infty \rangle = 0$  and  $\langle z_\infty \rangle = 1/[\mu_s (1 - \langle \cos \gamma \rangle)]$  give the coordinates of the center of symmetry of the statistical photon distribution. In particular, the coordinate  $\langle z_\infty \rangle$  can be interpreted as the average distance between consecutive, effectively isotropic scattering events, and its inverse is defined as the reduced scattering coefficient  $\mu'_s$ :

$$\mu'_s = \mu_s (1 - \langle \cos \gamma \rangle). \quad (7.33)$$

In the case of isotropic scattering,  $\langle \cos \gamma \rangle = 0$  and  $\mu'_s = \mu_s$ . In the case of forward scattering,  $\langle \cos \gamma \rangle = 1$  and  $\mu'_s = 0$ .

### 7.3.6 The $P_1$ equation and the standard diffusion equation (SDE)

We now reduce the  $P_1$  approximation to a single equation for the photon density  $U(\mathbf{r}, t)$ . From Eq. (7.27) we obtain  $\mathbf{J}(\mathbf{r}, t)$ :

$$\begin{aligned} \mathbf{J}(\mathbf{r}, t) &= -\frac{1}{v(\mu'_s + \mu_a)} \frac{\partial}{\partial t} \mathbf{J}(\mathbf{r}, t) - \frac{v}{3(\mu'_s + \mu_a)} \nabla U(\mathbf{r}, t) + \frac{1}{(\mu'_s + \mu_a)} \mathbf{S}_1(\mathbf{r}, t) \\ &= -\frac{3D}{v^2} \frac{\partial}{\partial t} \mathbf{J}(\mathbf{r}, t) - D \nabla U(\mathbf{r}, t) + \frac{3D}{v} \mathbf{S}_1(\mathbf{r}, t), \end{aligned} \quad (7.34)$$

where we have defined the diffusion coefficient  $D = v/[3(\mu'_s + \mu_a)]$ . By substituting this expression for  $\mathbf{J}(\mathbf{r}, t)$  in Eq. (7.26), we get:

$$\frac{\partial}{\partial t} U(\mathbf{r}, t) + v\mu_a U(\mathbf{r}, t) - \frac{3D}{v^2} \frac{\partial}{\partial t} \nabla \cdot \mathbf{J}(\mathbf{r}, t) - D\nabla^2 U(\mathbf{r}, t) + \frac{3D}{v} \nabla \cdot \mathbf{S}_1(\mathbf{r}, t) = S_0(\mathbf{r}, t). \quad (7.35)$$

From Eq. (7.26),  $\nabla \cdot \mathbf{J}(\mathbf{r}, t) = S_0(\mathbf{r}, t) - \frac{\partial}{\partial t} U(\mathbf{r}, t) - v\mu_a U(\mathbf{r}, t)$ . By substituting this expression and by rearranging the terms, we finally get the  $P_1$  equation for the photon density:

$$\begin{aligned} \nabla^2 U(\mathbf{r}, t) = & \frac{3}{v^2} \frac{\partial^2 U(\mathbf{r}, t)}{\partial t^2} + \frac{1}{D} \left( 1 + \frac{3D}{v} \mu_a \right) \frac{\partial U(\mathbf{r}, t)}{\partial t} + \frac{v\mu_a}{D} U(\mathbf{r}, t) \\ & - \frac{3}{v^2} \frac{\partial S_0(\mathbf{r}, t)}{\partial t} - \frac{1}{D} S_0(\mathbf{r}, t) + \frac{3}{v} \nabla \cdot \mathbf{S}_1(\mathbf{r}, t). \end{aligned} \quad (7.36)$$

By making a few assumptions, which are often satisfied in the case of light propagation in biological tissue, Eq. (7.36) reduces to the standard diffusion equation (SDE). The assumptions are the following:

- (1) Strongly scattering regime, or  $\mu_a \ll \mu'_s$ . This condition means that a photon, on the average, will undergo many effectively isotropic scattering events before being absorbed. In this case,  $3D\mu_a/v \equiv \mu_a/(\mu_a + \mu'_s) \ll 1$ , and the second term on the right hand side of Eq. (7.36) reduces to  $(1/D) \partial U(\mathbf{r}, t) / \partial t$ .
- (2) Time scale of the variations of  $U(\mathbf{r}, t)$  and  $S_0(\mathbf{r}, t)$  are much greater than the average time between collisions  $1/[v(\mu_a + \mu'_s)]$ . This condition can be expressed by the formal inequality:  $\partial / \partial t \ll v(\mu_a + \mu'_s) \equiv v^2 / (3D)$ . Consequently:

$$\frac{3}{v^2} \frac{\partial^2 U(\mathbf{r}, t)}{\partial t^2} \ll \frac{1}{D} \frac{\partial U(\mathbf{r}, t)}{\partial t}, \quad (7.37)$$

$$\frac{3}{v^2} \frac{\partial S_0(\mathbf{r}, t)}{\partial t} \ll \frac{1}{D} S_0(\mathbf{r}, t). \quad (7.38)$$

In the frequency-domain, where the harmonic time dependence is given by a factor  $\exp(-i\omega t)$ , the time derivative operator becomes a multiplication by  $-i\omega$ . Here,  $\omega$  is the angular modulation frequency of the intensity modulation (which should not be confused with the frequency of light). Consequently, this condition poses an upper limit to the modulation frequency given by  $\omega \ll v^2 / (3D)$ . In the case of biological tissues, the SDE usually breaks down at modulation frequencies on the order of 1 GHz.<sup>16</sup>

(3) The source term is isotropic, i.e.  $\mathbf{S}_1(\mathbf{r}, t) = 0$ .

With these assumptions, the  $P_1$  equation (Eq. 7.36) reduces to the standard diffusion equation:

$$\frac{\partial U(\mathbf{r}, t)}{\partial t} = D\nabla^2 U(\mathbf{r}, t) - v\mu_a U(\mathbf{r}, t) + S_0(\mathbf{r}, t), \quad (7.39)$$

and the photon flux  $\mathbf{J}(\mathbf{r}, t)$  is related to the photon density  $U(\mathbf{r}, t)$  by Fick's law:

$$\mathbf{J}(\mathbf{r}, t) = -D\nabla U(\mathbf{r}, t). \quad (7.40)$$

In the frequency-domain,  $\partial/\partial t \rightarrow -i\omega$  and the diffusion equation takes the form of the Helmholtz equation:

$$\left(\nabla^2 + k^2\right)U(\mathbf{r}) = -\frac{S_0(\mathbf{r})}{D}, \quad (7.41)$$

where  $k^2 = (i\omega - v\mu_a)/D$ .

### 7.3.7 Solution of the standard diffusion equation in the frequency-domain

The solution to the diffusion equation for a homogeneous, infinite medium containing a harmonically modulated point source of power  $P(\omega)$  at  $\mathbf{r} = 0$  is given by:<sup>33</sup>

$$U(r, \omega) = \frac{P(\omega)}{4\pi D} \frac{e^{ikr}}{r}. \quad (7.42)$$

The explicit expressions for the average photon density ( $U_{DC}$ ), and for the amplitude ( $U_{AC}$ ) and phase ( $\Phi$ ) of the photon-density wave are:<sup>34,25,35</sup>

$$U_{DC}(r) = \frac{P_{DC}}{4\pi D} \frac{e^{-r(v\mu_a/D)^{1/2}}}{r}, \quad (7.43)$$

$$U_{AC}(r, \omega) = \frac{P(\omega)}{4\pi D} \frac{e^{-r(v\mu_a/2D)^{1/2} \left[ \left( 1 + \frac{\omega^2}{v^2\mu_a^2} \right)^{1/2} + 1 \right]^{1/2}}}{r}, \quad (7.44)$$

$$\Phi(r, \omega) = r(v\mu_a/2D)^{1/2} \left[ \left( 1 + \frac{\omega^2}{v^2\mu_a^2} \right)^{1/2} - 1 \right]^{1/2} + \Phi_s, \quad (7.45)$$

where  $\Phi_s$  is the source phase in radians. Analytical solutions in the frequency-domain have also been reported for a semi-infinite medium,<sup>25,35,36</sup> infinite slab,<sup>37</sup> cylindrical and spherical geometries.<sup>37</sup> Equations (7.39) and (7.41) refer to

homogeneous media. For quantitative tissue spectroscopy and oximetry (section 7.4), one typically assumes that tissues are macroscopically homogeneous, so that Eqs. (7.39) and (7.41) are applicable. By contrast, optical imaging of tissues (section 7.5) aims at measuring the spatial distribution of the tissue optical properties, and Eq. (7.39) must be generalized to account for the spatial dependence of  $\mu_a$  and  $D$ .

## 7.4 Tissue spectroscopy and oximetry

### 7.4.1 Optical properties of biological tissue

As discussed in section 7.3.1, the propagation of light inside biological tissues can be described in terms of flow of photons. In this perspective, the light source injects a given number of photons per unit time, per unit volume, per unit solid angle into a specific tissue location and these photons travel inside the tissue along certain trajectories. The collective motion of photons along these trajectories is called *photon migration*. While traveling inside tissues, photons can undergo a number of different processes, such as absorption, elastic scattering, inelastic scattering (for instance, dynamic light scattering and Raman Scattering), and fluorescence. In this Chapter, we consider only absorption (section 7.4.1.1) and elastic scattering (section 7.4.1.2) events. The scattering process from non-stationary scattering centers in tissues (cells, cellular organelles, etc.), which strictly speaking is an inelastic process, involves such small wavelength changes that it is also referred to as quasi-elastic scattering. Quasi-elastic scattering is the basis for dynamic light scattering,<sup>38</sup> diffusing-wave spectroscopy,<sup>39</sup> photon correlation spectroscopy,<sup>40</sup> and laser Doppler flowmetry.<sup>41</sup> When a photon is absorbed, it disappears and transfers its energy to the absorbing center. When a photon is elastically (or quasi-elastically) scattered, its direction of propagation changes, while its wavelength remains essentially unchanged. By contrast, Raman scattering and fluorescence processes cause larger photon wavelength changes related to the involvement of vibrational energy levels.

#### 7.4.1.1 Absorption

The main absorbers of near-infrared (NIR) light in blood-perfused tissues are oxy-hemoglobin, deoxy-hemoglobin, and water. Their absorption spectra between 300 and 1500 nm are shown in Fig. 7.4, which is obtained from compiled absorption data for water<sup>42</sup> and hemoglobin.<sup>43</sup> In Fig. 7.4, the concentrations of oxy-hemoglobin and deoxy-hemoglobin are assumed to be 50  $\mu\text{M}$ , which is a typical value in blood-perfused tissues. We observe that the absorption coefficients reported in Fig. 7.4 are defined to base  $e$ , and those for hemoglobin refer to a complete molecule (four heme groups). The so-called “medical spectral window” extends approximately from 700 to 900 nm, where the absorption of light shows a minimum (see Fig. 7.4). As a result, light in this

spectral window penetrates deeply into tissues, thus allowing for non-invasive investigations. The optical penetration depth into tissues is limited, at shorter wavelengths, by the hemoglobin absorption, and at longer wavelengths by the water absorption. Other NIR absorbers in tissues that may be important in particular cases include myoglobin, cytochrome oxidase, melanin, and bilirubin.

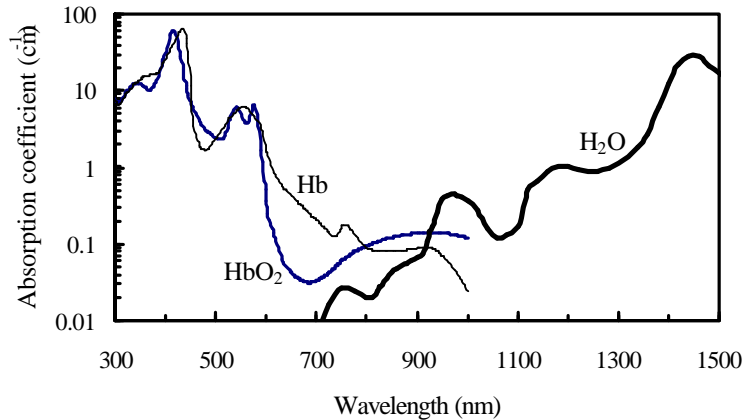


Fig. 7.4. Absorption spectra of the three dominant near-infrared chromophores in tissues, namely oxy-hemoglobin ( $\text{HbO}_2$ ), deoxy-hemoglobin ( $\text{Hb}$ ), and water ( $\text{H}_2\text{O}$ ). The absorption coefficient is defined to base  $e$ . The concentrations of  $\text{Hb}$  and  $\text{HbO}_2$  are both assumed to be  $50 \mu\text{M}$ , a typical value for blood-perfused tissues. These spectra are obtained from compiled absorption data for water<sup>42</sup> and hemoglobin.<sup>43</sup>

The absorption properties of tissue are described by the absorption coefficient ( $\mu_a$ ), which is defined as the inverse of the average photon path length before absorption. From this definition, it follows that  $1/\mu_a$  is the average distance traveled by a photon before being absorbed. In the NIR, typical values of  $\mu_a$  in tissues range from  $0.02$  to  $0.30 \text{ cm}^{-1}$ . The photon mean free path for absorption thus ranges between about 3 and 50 cm.

#### 7.4.1.2 Scattering

The scattering properties are mainly determined by the size of the scattering particles relative to the wavelength of light, and by the refractive index mismatch between the scattering particles and the surrounding medium. In biological tissues, the scattering centers are cells and cellular organelles. In the medical spectral window (700-900 nm), cellular organelles have dimensions comparable to the wavelength, and their index of refraction is relatively close to that of the cytosol and extracellular fluid. As a result, light scattering in tissue is mainly forward directed (i.e. the scattering angle  $\gamma$  introduced in section 7.3.2 is less than  $90^\circ$ ) and shows a weak wavelength dependence.

As discussed in sections 7.3.1 and 7.3.5, the scattering properties of tissues are described by two parameters; (1) the scattering coefficient ( $\mu_s$ ), defined as the inverse of the average photon path length between successive

scattering events, and (2) the average cosine of the scattering angle ( $f_1 = \langle \cos\gamma \rangle$ ). From the definition of  $\mu_s$ , it follows that  $1/\mu_s$  is the average distance traveled by a photon between successive scattering events, as shown by Eq. (7.28). Even though each scattering event is mainly forward directed, after a number of collisions a photon loses memory of its original direction of propagation. Under these conditions, we can say that the photon has experienced an effectively isotropic scattering event. As discussed in section 7.3.5, the reduced scattering coefficient [ $\mu_s' = (1 - f_1) \mu_s$ ] represents the inverse of the average distance over which the direction of propagation of a photon is randomized. In other words, we can say that  $1/\mu_s'$  is the average distance between effectively isotropic scattering events. Note that  $\mu_s'$  coincides with  $\mu_s$  in the case of isotropic scattering ( $f_1 = 0$ ). Typical values of  $\mu_s'$  in biological tissues range from 2 to  $20 \text{ cm}^{-1}$ , while  $f_1$  is typically 0.8-0.9 (so that  $\mu_s'$  is about one order of magnitude smaller than  $\mu_s$ ).<sup>44</sup> The average distance traveled by a photon in tissues before losing memory of its initial direction of propagation is typically a few millimeters or less.

#### 7.4.2 Absorption spectroscopy of tissues

Since  $\mu_s'$  is typically much larger than  $\mu_a$ , NIR light propagation in tissue is dominated by scattering. This is one of the conditions discussed in section 7.3.6 for the validity of the diffusion equation [Eq. (7.39)]. The frequency-domain solution given by Eq. (7.42) provides a quantitative description of photon migration in an infinite medium with uniform optical properties. However, biological tissues are neither infinite, nor homogeneous. With regard to tissue inhomogeneity, Eq. (7.42) is a reasonable approximation as long as the characteristic size of the tissue inhomogeneities (for instance, muscle fibers, blood vessels, etc.) is small compared with the source-detector separation. A second problem is determined by the boundary conditions that are associated with the finite volume of the investigated tissue. In a reflectance geometry, where the source and the detector are located on the same side of the tissue, one typically applies the semi-infinite boundary condition. This condition implies that the tissue acts as an effective half-space, which is a reasonable assumption if the tissue depth is greater than the optical penetration depth (which is typically on the order of 2-3 cm or less). This assumption is not valid in a transmission geometry (where the source and the detector are located on opposite sides of the tissue), or in the case of a small tissue volume. In these cases, the application of more appropriate boundary conditions (such as a slab, cylinder, or sphere) may be needed.<sup>37</sup>

Tissue spectroscopy aims at determining certain properties of the investigated tissue volume (for example, the oxygenation or the hemoglobin concentration of a muscle) on the basis of measurement of the optical properties (absorption and scattering) of the tissue. Since the absorption coefficient of

tissues is due to a number of chromophores (oxy-hemoglobin, deoxy-hemoglobin, water, cytochrome oxidase, melanin, bilirubin, lipids, etc.), multi-wavelength measurements have been employed to determine the relative contributions of each chromophore. The basic idea is that the contribution to  $\mu_a$  from the  $i$ -th chromophore can be written as the product of the extinction coefficient ( $\epsilon_i$ ) times the concentration ( $C_i$ ) of that chromophore. As a result, in the presence of  $N$  chromophores, the absorption coefficient  $\mu_a$  at wavelength  $\lambda_j$  is given by:

$$\mu_a(\lambda_j) = \sum_{i=1}^N \epsilon_i(\lambda_j) C_i. \quad (7.46)$$

If the extinction spectra  $\epsilon_i(\lambda)$  of all  $N$  species are known, the concentrations  $C_i$  can be determined by measuring  $\mu_a$  at  $N$  or more wavelengths, so that the linear system of Eq. (7.46) is fully determined. This approach requires that  $\mu_a$  be measured independently of  $\mu_s$ . In the frequency-domain, Eqs. (7.43)-(7.45), or the corresponding equations for semi-infinite or other geometries, can be used to quantitatively measure  $\mu_a$  and  $\mu_s$ .<sup>36</sup> The spatial<sup>10</sup> or the frequency<sup>17</sup> dependence of the DC intensity, AC amplitude, and phase can also be effectively used for *in vivo* tissue spectroscopy. It is worth noting that this approach to tissue spectroscopy yields quantitative, absolute values of the concentration of chromophores in tissue.

### 7.4.3 Near-infrared tissue oximetry

In many cases, the absorption spectra of tissues can be well described by considering only three chromophores, namely oxy-hemoglobin, deoxy-hemoglobin, and water. For example, Fig. 7.5 shows the absorption coefficients of human muscle (forearm) and brain (forehead) measured at eight NIR wavelengths (squares) under resting conditions. The lines in Fig. 7.5 are the best fit absorption spectra corresponding to a linear combination of the water, oxy-hemoglobin, and deoxy-hemoglobin extinction spectra. In the fits, the water concentration (by volume) is assumed to be 75% for the muscle, and 80% for the brain,<sup>45</sup> while the concentrations of oxy-hemoglobin ( $[\text{HbO}_2]$ ) and deoxy-hemoglobin ( $[\text{Hb}]$ ) are the fitting parameters. The best fit spectra of Fig. 7.5 yield values of  $[\text{HbO}_2]$  and  $[\text{Hb}]$  of 58  $\mu\text{M}$  and 26  $\mu\text{M}$ , respectively, in the muscle, and 30  $\mu\text{M}$  and 10  $\mu\text{M}$ , respectively, in the brain. Consequently, the measured hemoglobin saturation in the muscle is 69%,<sup>24</sup> while in the brain it is 75%.<sup>46</sup> The good fit between the experimental data and the three-component absorption spectra indicates that oxy- and deoxy-hemoglobin are indeed the dominant absorbing species over the wavelength range considered (630-840 nm) (water absorption only introduces a relatively small correction at these wavelengths). This result allows for measurements of the oxygen saturation of hemoglobin in tissues using just two wavelengths. The possibility of using dual wavelength optical measurements for blood oximetry have been known for a

long time,<sup>47</sup> and it is exploited by pulse oximeters to measure the arterial saturation.<sup>48</sup> The novelty introduced by frequency-domain and time-domain spectroscopy is the capability of performing absolute tissue oximetry.<sup>23,49</sup>

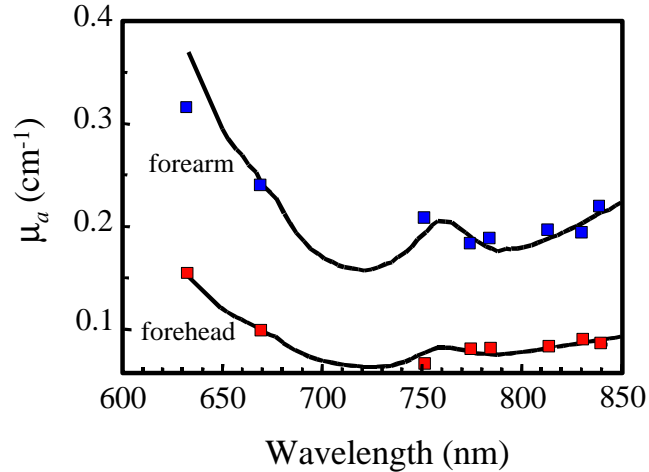


Fig. 7.5. Quantitative absorption spectroscopy of tissues *in vivo*.<sup>24,46</sup> The squares represent the eight-wavelength spectra measured with frequency-domain spectroscopy in the skeletal muscle and in the forehead (according to the label) of human subjects. The lines are best fits using a linear combination of the extinction spectra of oxy-hemoglobin, deoxy-hemoglobin, and water.

The two wavelengths  $\lambda_1$  and  $\lambda_2$  for near-infrared oximetry are usually chosen such that  $\lambda_1 < \lambda_{\text{iso}} \leq \lambda_2$ , where  $\lambda_{\text{iso}}$  is the NIR isosbestic wavelength at which the extinction coefficients of oxy- and deoxy-hemoglobin have the same value ( $\lambda_{\text{iso}}$  is about 800 nm as can be seen in Fig. 7.4). This choice maximizes the sensitivity of the optical measurement to changes in the tissue oxygenation. The measurement of  $\mu_a$  at two wavelengths translates Eq. (7.46) into a linear system of two equations (one per each wavelength) and two unknowns (namely, the concentrations of oxy-hemoglobin and deoxy-hemoglobin in the tissue). Its solution gives the oxy- and deoxy-hemoglobin concentrations, which in turn yield the total hemoglobin concentration ( $\text{THC} = [\text{HbO}_2] + [\text{Hb}]$ ) and the tissue saturation ( $\text{StO}_2 = [\text{HbO}_2]/\text{THC}$ ). Figures 7.6(a), (b), and (c) show typical traces of total hemoglobin concentration and tissue saturation measured with the frequency-domain tissue oximeter described in section 7.2.6 (see Fig. 7.2). Panels (a) and (b) of Fig. 7.6 refer to measurements on the brachioradialis muscle (forearm) of a human subject during arterial and venous occlusion, respectively, while panel (c) refers to a measurement on the vastus lateralis muscle (thigh) during treadmill exercise.<sup>50</sup>

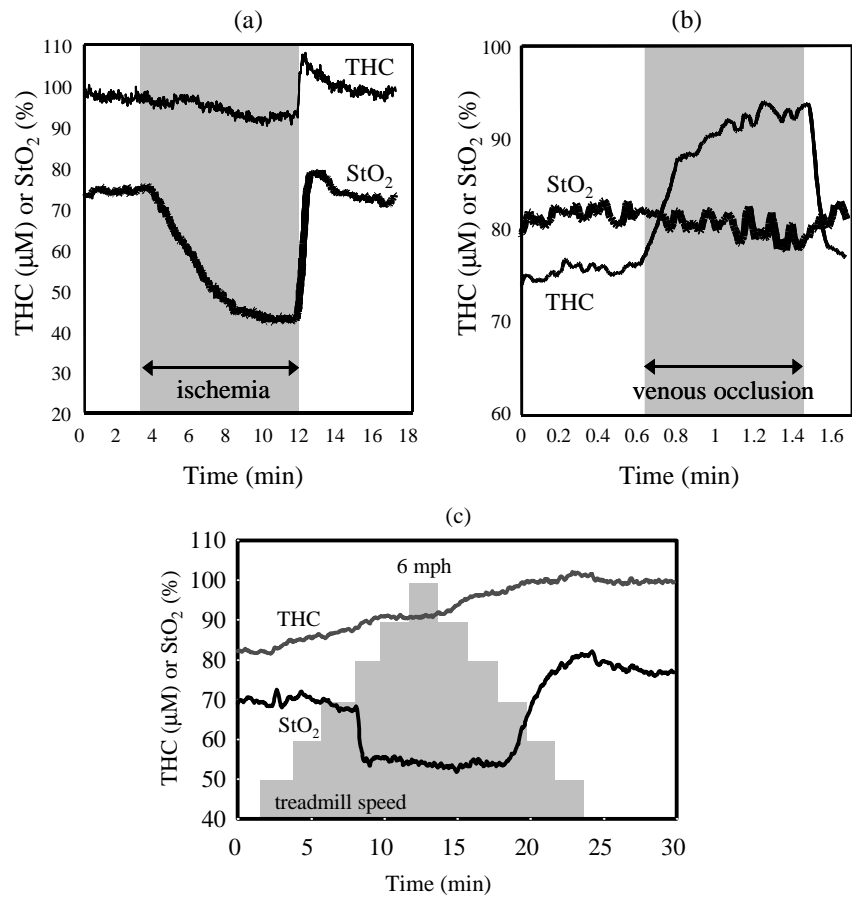


Fig. 7.6. Temporal traces of optically measured total hemoglobin concentration ( $\text{THC} = [\text{HbO}_2] + [\text{Hb}]$ ) and tissue saturation ( $\text{StO}_2$ ) in human subjects. The measurements were conducted on a forearm muscle during (a) arterial or (b) venous occlusion, and (c) on a calf muscle during treadmill exercise. In panel (c), the step function represent the treadmill speed, which was changed by steps of 1 mph every 2 minutes.<sup>50</sup> Running started at a speed of 4 mph. The frequency-domain measurements allow for absolute y-axis readings

The two wavelengths employed in this particular case are 758 and 830 nm, and the acquisition time per data point is 1.28 s. The traces appear in real time on the computer screen during the examination. We stress again that the y-axes for hemoglobin concentration and saturation are quantitative and absolute. Figure 7.6(a) shows that the tissue desaturation during ischemia results from a rate of decrease of  $[\text{HbO}_2]$  that is equal to the rate of increase of  $[\text{Hb}]$  (because the total hemoglobin concentration THC remains constant during ischemia). The rate of conversion of  $\text{HbO}_2$  to  $\text{Hb}$  can be used to quantify the muscle oxygen consumption.<sup>51,52</sup> The main effect of the venous occlusion [Fig. 7.6(b)] is to increase the hemoglobin concentration, as a result of blood accumulation. In

fact, while the arterial inflow is unaffected by the venous occlusion, the venous outflow is blocked. The initial rate of increase of THC during venous saturation can be used to measure the muscle blood flow.<sup>53-56</sup> Figure 7.6(c) provides an example of an oxygenation and hemodynamics study *in vivo* during muscle exercise, with potential applications in the area of sports medicine.<sup>50</sup>

Near-infrared oximetry lends itself to measurements on the human head as well. Figure 7.7(a) shows the arrangement of optical fibers on the forehead of a human subject. The cerebral oxygenation may be varied by changing the fraction of oxygen inspired by the subject. The resulting changes in the cerebral tissue oxygenation ( $StO_2$ ) are reported in Fig. 7.7(b). Figure 7.7(b) also shows a comparison between two traces of arterial saturation ( $SaO_2$ ); one is measured with a commercial pulse oximeter, while the other is measured with a frequency-domain tissue oximeter.<sup>46</sup> Both instruments use the oscillatory components of the optical signals at the frequency of the heartbeat (which are directly associated with the arterial pulsation, and therefore with arterial blood volume). The key difference is that while the pulse oximeter applies an empirical calibration to translate the pulsatile components of the optical densities into a reading of arterial saturation, the frequency-domain oximeter directly measures the pulsatile components of the absorption coefficients and quantifies the arterial saturation by applying Eq. (7.46).<sup>46</sup>

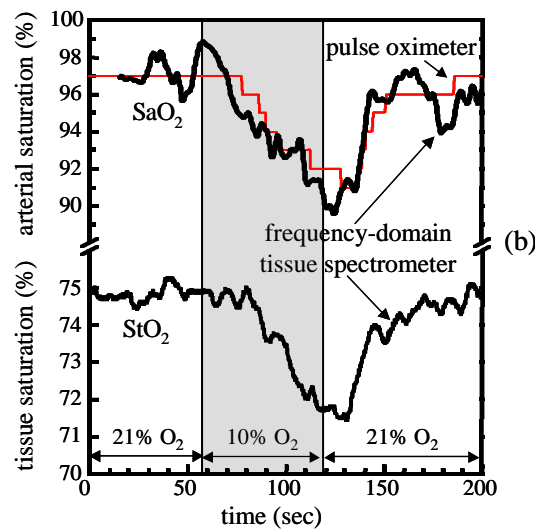


Fig. 7.7. (a) Application of optical fibers to the forehead of a human subject for frequency-domain brain oximetry. (b) Temporal traces of arterial saturation ( $SaO_2$ ) measured systemically (on a finger) by a pulse oximeter and locally (on the forehead) by a frequency-domain oximeter that also measured the cerebral tissue saturation ( $StO_2$ ).<sup>46</sup> The fraction of oxygen inspired by the subject was varied between 21% and 10% (by volume) as indicated in the figure.

The lack of discomfort associated with near-infrared measurements *in vivo*, and their non-invasive character, renders near-infrared tissue oximetry a suitable technique for newborn infants. For instance, Fig. 7.8 shows a comparison between the systemic reading of arterial saturation (with a pulse oximeter attached to a toe), and the cerebral oxygenation measured locally with a frequency-domain tissue oximeter. In this case, the decrease in the measured oxygenation was induced by a controlled decrease in the fraction of inspired oxygen. The arterial saturation and the cerebral saturation show a qualitatively similar trend. However, a local cerebral deoxygenation would be detected only by the NIR cerebral measurement. The manual application of the optical probe

shown in Fig. 7.8(a) can be replaced by a flexible headband<sup>57,58</sup> or by an infant cap for continuous long-term monitoring.

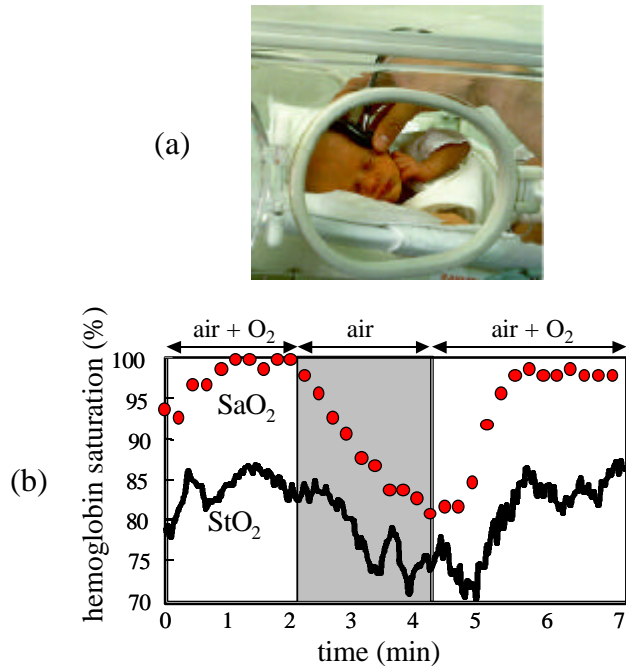


Fig. 7.8. Frequency-domain, near-infrared oximetry of the newborn infant brain. (a) Photograph showing the application of a flexible optical probe to the infant's head. (b) Temporal traces of cerebral tissue saturation ( $StO_2$ ) measured with frequency-domain optical oximetry, and systemic arterial saturation ( $SaO_2$ ) measured with a pulse oximeter at an infant's toe. Deoxygenation is achieved by a controlled reduction in the fraction of inspired oxygen (in collaboration with G. P. Donzelli and S. Pratesi, University of Florence, Italy).

#### 7.4.4 Measurements of optical scattering in tissues

Traditionally, optical studies have been targeted at measurements of the absorption properties of tissues. The strong scattering of light in tissue constitutes a complication in quantitative absorption spectroscopy. However, it has recently been suggested that the reduced scattering coefficient itself may provide information about physiologically relevant parameters. For instance, it has been shown that mitochondria are the main source of light scattering in the liver, and possibly in other tissues as well.<sup>59</sup> Since a number of metabolic processes related to cellular respiration occur in the mitochondria, the reduced scattering coefficient may be related to the cellular activity and viability. Furthermore, some studies have shown a correlation between blood glucose concentration and the reduced scattering coefficient of tissue.<sup>60-62</sup> This correlation is suggested by the fact that the scattering properties of tissues depend

on the mismatch between the refractive indices of the scattering centers (cells, cellular organelles) and the host medium (extracellular fluid, cytosol). Since the index of refraction of the extracellular fluid is sensitive to glucose concentration, it is a plausible hypothesis that  $\mu_s'$  would be affected by the blood glucose concentration. *In vitro* studies have predicted that the sensitivity of  $\mu_s'$  to the blood glucose level should be adequate to monitor glucose concentrations within the physiological range<sup>61</sup> (80-120 mg/dl in blood). This prediction is confirmed by Fig. 7.9, which shows a trace of  $\mu_s'$  measured by frequency-domain NIR spectroscopy on the thigh muscle of a healthy 26-year old male subject during a glucose tolerance test.<sup>61</sup> The reduced scattering coefficient decreases as the blood glucose increases, because of the glucose-induced reduction in the refractive index mismatch between the scattering centers and the host fluid. However, this kind of measurement yields only a relative determination of glucose concentration.

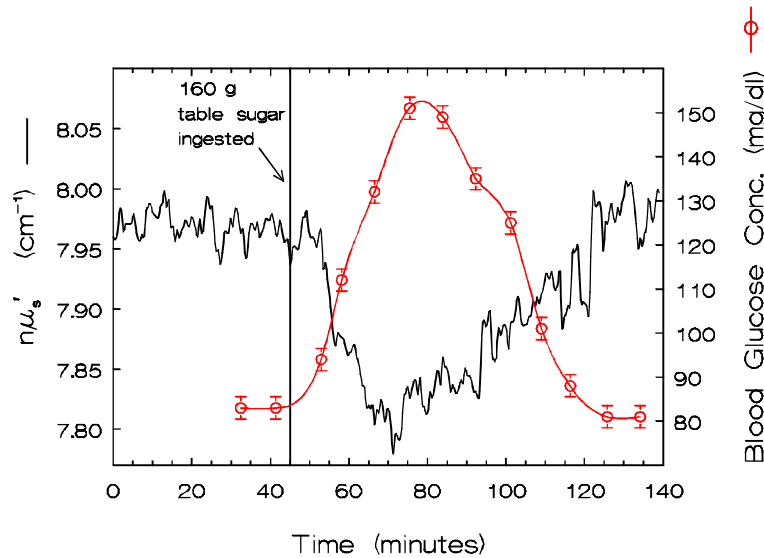


Fig. 7.9. Comparison between the blood glucose concentration dynamics and the temporal evolution of the reduced scattering coefficient ( $\mu_s'$ ) measured on the thigh muscle by frequency-domain spectroscopy during a glucose tolerance test.<sup>61</sup> The diffusion model is not able to separate  $\mu_s'$  from the refractive index  $n$  of the tissue [in Eq. (7.42)  $n$  and  $\mu_s'$  are coupled in the expression for  $D = v/[3(\mu_s' + \mu_a)] \cong c/(3n \mu_s')$ , where  $c$  is the speed of light in vacuum], so that the y-axis reports the product  $n \mu_s'$ .

Furthermore, there are a number of additional factors, such as changes in temperature and in pH, that yield variations in  $\mu_s'$  that compete with the glucose-induced effects. Theoretical and experimental studies of the optical properties of the human sclera (the white outer coat enclosing the eyeball) have also shown a significant scattering change induced by glucose and by other osmotically active species.<sup>63</sup> While the monitoring of glucose concentration by NIR spectroscopy,

at the present stage of development, is far from being clinically applicable, it nevertheless points out the diversity of potential diagnostic applications of medical optics.

## 7.5 Optical imaging of tissues

### 7.5.1 General concepts

Optical imaging relies on its sensitivity to optical properties of tissues, namely absorption and scattering. Consequently, the contrast in NIR imaging originates from spatial variations in the optical absorption and scattering properties of the tissue. These spatial variations can be due to a local change in hemoglobin concentration or saturation (for instance, a hematoma or heterogeneous vascularization, blood flow, or oxygenation), a localized change in the tissue architecture (for example, a result of micro calcifications) or the concentration of cellular organelles. In any case, NIR imaging is sensitive to physical properties of tissues that are different than those probed by current diagnostic imaging modalities such as x-ray tomography (mass density, atomic number), ultrasound (acoustic impedance), magnetic resonance imaging (proton density, nuclear relaxation times), and positron emission tomography (accumulation of a radioactive tracer). In this sense, NIR imaging is not necessarily an alternative to these imaging modalities, but could constitute an adjunct technique providing an effective complement to existing methods. We point out here that the promise of optical tomography is not in achieving a high spatial resolution (which is intrinsically limited by the diffusive nature of light propagation in tissues), but rather in achieving high contrast and specificity.

NIR tissue imaging aims at generating spatial maps that display either structural or functional properties of tissues. Since optical imaging studies the spatial distribution of the optical properties, Eq. (7.39) must be replaced with the diffusion equation for inhomogeneous media:

$$\frac{\partial U(\mathbf{r}, t)}{\partial t} - \nabla \cdot D(\mathbf{r}) \nabla U(\mathbf{r}, t) + \nu \mu_a(\mathbf{r}) U(\mathbf{r}, t) = q(\mathbf{r}, t). \quad (7.47)$$

Equation (7.47) can be used to solve the forward problem, which consists of finding the photon density  $U(\mathbf{r}, t)$  corresponding to a given spatial distribution of the optical properties and of the photon sources. Analytical solutions of Eq. (7.47) are available only for a few inhomogeneous cases such as those of spherical<sup>33</sup> and cylindrical<sup>64</sup> inclusions. For arbitrary inhomogeneous cases, Eq. (7.47) can be solved using numerical methods such as the finite difference method (FDM)<sup>65</sup> or the finite element method (FEM).<sup>66</sup> Alternatively, a perturbation expansion in  $\mu_a$  and  $D$  leads to a solution of Eq. (7.47) in terms of a volume integral involving the appropriate Green's function.<sup>67,68</sup> Besides using diffusion theory, the case of inhomogeneous media can also be treated with

stochastic methods such as Monte Carlo simulations<sup>69,70</sup> or lattice random walk models.<sup>71</sup>

The goal of imaging is to solve the inverse problem, which consists of determining the spatial distribution of  $\mu_a$  and  $D$  (or  $\mu_a$  and  $\mu_s'$ ) within a volume  $V$ , from optical measurements at the boundary of  $V$ . Perturbation methods linearize the problem by keeping only the linear term in an expansion of the change in the measured quantities induced by a perturbation in the optical properties. The inverse problem reduces to inverting the Jacobian (i.e., the first derivative matrix) of the measured quantities with respect to the optical properties. The Jacobian matrix can be estimated using a Monte Carlo<sup>72</sup> or an analytical<sup>67,68</sup> model. The main practical disadvantage of the perturbation method is that it requires a difference between measurements with and without the perturbation. For *in vivo* applications, this is sometimes impractical, save the cases of dynamical perturbations such as those induced by evoked cerebral activity or by the injection of optical contrast agents.<sup>73</sup>

Non-linear approaches are based on minimization of the distance (in measurement space) between the measured data and the projection of the distribution of optical properties onto the measurement space (according to the forward problem). The minimization process involves repeated iterations, so the computational speed of the forward model is a relevant factor. One example of a non-linear approach is the Newton-Raphson scheme for minimization, which has been used in conjunction with an FEM forward model to do optical tomography.<sup>74-76</sup> The above mentioned methods usually require relatively long computation times that render them unsuitable for real-time imaging. For applications where real time information is important, simplified algorithms based on back projection<sup>77-79</sup> or on direct projection for 2-D mapping<sup>80</sup> have been proposed. A recent and comprehensive review of medical optical imaging can be found in Ref. 30.

## **7.5.2 Non-invasive optical imaging of the human brain**

### **7.5.2.1 Detection of intracranial hematomas**

Several studies have demonstrated that near-infrared light propagates through the intact skull.<sup>81-83</sup> One technique using continuous wave (CW) light (wavelength: 760 nm, source-detector separation: 3.5 cm) has been used to detect intracranial hematomas in head-injured patients.<sup>84</sup> This is based on the fact that there is a greater concentration of hemoglobin in a hematoma with respect to normal brain tissue, resulting in a higher absorption of NIR light. A significant asymmetry between the optical signals collected over the two hemispheres will indicate a condition that could possibly be related to the presence of a hematoma. This technique is not aimed at displaying optical images of the brain. Rather, it involves a comparison of optical measurements at two different brain locations. In this sense, although this is not a true imaging technique, spatially-resolved measurements are involved.

Another approach, using a hybrid of CW and frequency-domain techniques has been employed to perform real-time imaging (image acquisition rate: 5.2 Hz) of an experimental brain hemorrhage in a piglet model.<sup>85</sup> Figure 7.10 shows the optical image recorded non-invasively through the intact scalp and skull immediately following the subcortical injection (depth of injection: 1.2 cm) of 0.5 cc of autologous blood. In Fig. 7.10, a photograph of a brain slice obtained after autopsy is superimposed to the near-infrared image to show the geometrical relationship between the optical image and the piglet brain. The optical image was obtained by linearly combining the readings from ten source-detector pairs according to a linear back-projection scheme.<sup>85</sup> While this scheme is computationally fast, it does not lead to quantitative readings, so that the absorption scale in Fig. 7.10 is qualitative (i.e., the image gives reliable spatially-resolved information on whether the absorption increases or decreases, but the absorption changes are not accurately quantified). The lack of quantitative capabilities in optical imaging of tissues is a general shortcoming of back-projection schemes.

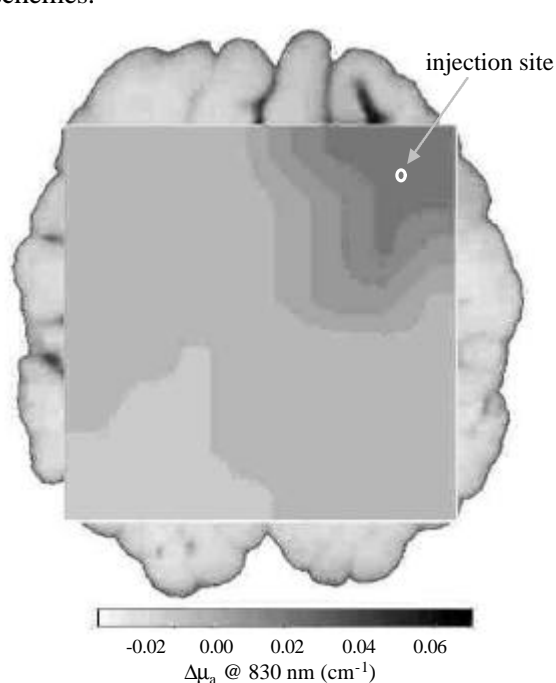


Fig. 7.10. Optical absorption image of a  $4 \times 4 \text{ cm}^2$  area of the piglet brain, measured non-invasively immediately after the subcortical injection of 0.5 cc of blood.<sup>85</sup> The injection site is indicated by the white circle. A picture of a brain slice taken after autopsy is superimposed to the optical image to show the geometrical relationship between the imaged area and the piglet brain. One can see the increased optical absorption over the area surrounding the injection site, which corresponds to the subcortical hemorrhage.

### 7.5.2.2 Functional imaging of the brain

The relationship between neuronal activation and local cerebral hemodynamics is provided by neurovascular coupling.<sup>86,87</sup> In the brain, local blood flow is continuously adjusted according to functional activity and metabolic demand. This adjustment occurs due to the vasomotor action of the cerebral arteries and arterioles. Both of the leading methods in functional neuroimaging, positron emission tomography (PET) and functional magnetic resonance imaging (fMRI), use neurovascular coupling to assess brain activity. Electroencephalography (EEG) and magnetoencephalography (MEG), on the other hand, can measure the fast (latency: 50-100 ms) electrical and magnetic signals directly related to neural activation. The spatial localization of the signals detected by EEG and MEG is problematic, however, because these techniques are sensitive to the whole brain. Near-infrared (NIR) imaging shows promise of being a unique technique, since it is the only existing modality that is sensitive to both ends of the neurovascular coupling, namely the neuronal activity and the vascular response. *In vitro* optical measurements on neurons have shown that neuronal activity is associated with an increase in light scattering, induced by a change in the index of refraction of the neuronal membranes.<sup>88,89</sup> In the last few years, several attempts have been made to measure such light scattering changes in human subjects *in vivo* and non-invasively. Using a frequency-domain system, G. Gratton *et al.*<sup>90</sup> have reported a transient increase in the pathlength of light in the visual cortex with a latency of 50-100 ms following the onset of visual stimulation. This signal shows a time course consistent with the electrophysiological response measured with EEG.

It has been proven that the hemodynamic changes monitored with NIR spectroscopy correlate with the activation state of the cortex in response to a stimulus. In fact, studies combining PET and fMRI with NIRS were able to demonstrate that the optically measured oxy- and total hemoglobin changes correspond to regional cerebral blood flow increases as measured by PET,<sup>91,92</sup> whereas deoxy-hemoglobin changes correspond to the BOLD signal measured by fMRI.<sup>93,94</sup> The circulatory effect of functional activation is an increase in cerebral blood flow (CBF) (higher blood volume and blood velocity) resulting from an increase in oxygen consumption. An increase in CBF that overcompensates the increase in oxygen consumption accounts for the observed decrease in the cerebral deoxy-hemoglobin concentration.<sup>95</sup>

Local cerebral studies are just a first step toward optical brain imaging. The key to functional brain imaging is a fast acquisition rate, which is required by the relatively short latency of the neural activation (~0.1 s) and the evoked hemodynamic signal (1-5 s). For structural brain imaging, the requirement of a fast acquisition time is not as important as for functional imaging. Several groups have reported non-invasive optical brain imaging with acquisition times per image of 3-5 s,<sup>96,97</sup> <30 s,<sup>98</sup> 2.5 min,<sup>99</sup> several hours,<sup>57,58</sup> and not-quantified “slow data acquisition rate”<sup>100</sup> and “long measurement times.”<sup>94</sup> Faster optical imaging approaches, suitable for non-invasive functional brain imaging, have

been recently reported with image acquisition times of 500 ms<sup>101</sup> and 160 ms.<sup>79</sup> Non-invasive optical studies of the brain are reviewed in Ref. 102.

Figure 7.11 shows the results of a functional brain imaging study that used a multi-channel frequency-domain optical instrument (a modified version of Model No. 96208, ISS, Inc., Champaign, IL, shown in Fig. 7.2).<sup>79</sup> The optically measured maps of cerebral deoxy-hemoglobin concentration show the activated cortical area during voluntary hand tapping. Image reconstruction was based on a linear superposition of the optical signals from ten source-detector pairs. The fast image acquisition rate (6.25 Hz) leads to on-line, continuous optical mapping of the cerebral cortex during the examination. Figure 7.11 shows one optical image every ten measurements (i.e., every 1.6 s) for space reasons. The real-time movie of the cerebral activation recorded with near-infrared imaging can be viewed in Ref. 79.

Currently, most optical functional studies of the brain have been based on continuous wave (CW) spectroscopy. Even Figure 7.11 shows results based on the DC component of the measured amplitude-modulated signal. The reason for the more common use of CW data in optical brain imaging is twofold. (1) The study of cerebral activation requires the measurement of changes in the optical signals that correlate with brain activity. Therefore, even relative readings, i.e. changes from an arbitrary initial value, yield meaningful information. (2) The absolute measurement capability afforded by time-resolved methods requires the application of a physical model for light propagation inside tissues. An accurate model for the highly inhomogeneous and geometrically irregular case of the human head is yet to be achieved. However, there are a few exceptions to the use of CW spectroscopy for optical studies of the brain.<sup>98,99,103,104</sup> These studies show that even without absolute measurements, time-resolved data can be extremely valuable in optical studies of the human brain. In fact, the additional information content of time-resolved data (the phase in the frequency-domain, the time-of-flight distribution in the time-domain) may lead to more effective approaches to human brain studies, for instance by affording the optimization of the spatial region of sensitivity, and the maximization of the sensitivity to localized absorption and scattering changes.

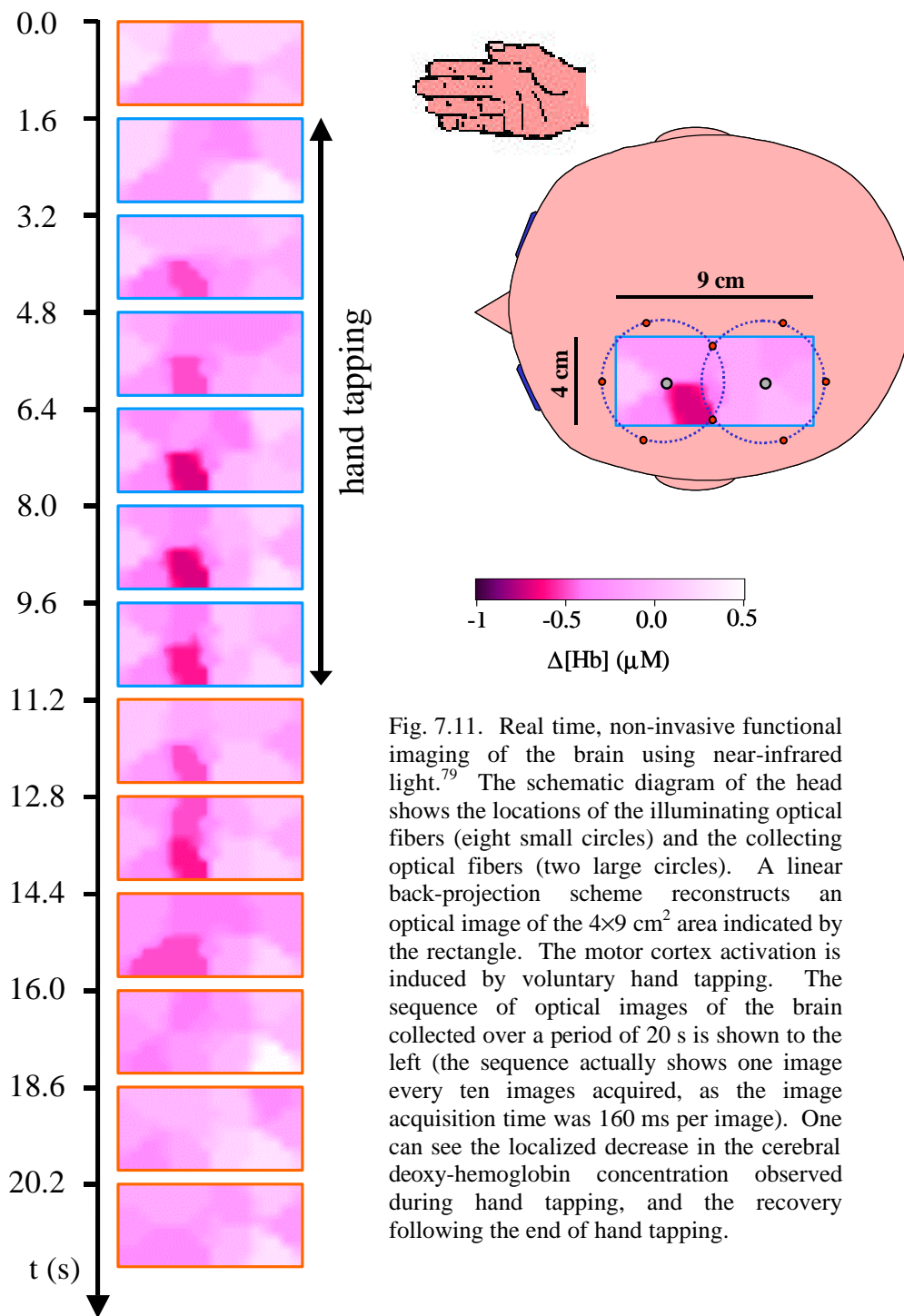


Fig. 7.11. Real time, non-invasive functional imaging of the brain using near-infrared light.<sup>79</sup> The schematic diagram of the head shows the locations of the illuminating optical fibers (eight small circles) and the collecting optical fibers (two large circles). A linear back-projection scheme reconstructs an optical image of the  $4 \times 9 \text{ cm}^2$  area indicated by the rectangle. The motor cortex activation is induced by voluntary hand tapping. The sequence of optical images of the brain collected over a period of 20 s is shown to the left (the sequence actually shows one image every ten images acquired, as the image acquisition time was 160 ms per image). One can see the localized decrease in the cerebral deoxy-hemoglobin concentration observed during hand tapping, and the recovery following the end of hand tapping.

### 7.5.3 Optical mammography

From a practical point of view, the human breast lends itself to near-infrared tissue spectroscopy and imaging. In fact, it is easily accessible and its relatively low hemoglobin concentration (10-20  $\mu\text{M}$ )<sup>105,106</sup> determines near-infrared absorption coefficients ( $\sim 0.02\text{-}0.04 \text{ cm}^{-1}$ ) that account for a deep optical penetration depth and the optical transmission through the whole breast. Furthermore, there is much appeal in the possibility of detecting breast cancer using a non-invasive method that does not involve ionizing radiation. The optical detection of breast cancer may rely on the perturbations induced by cancer on the host tissue rather than on a direct detection of optical signatures associated with cancer cells.<sup>107</sup> These perturbations include angiogenesis,<sup>107,108</sup> alterations to the blood flow and oxygenation<sup>108</sup> and fibroblast proliferation,<sup>107</sup> which may yield modifications to the optical scattering and absorption properties. However, it is not known whether these cancer-induced optical perturbations can lead to an effective optical approach to breast cancer detection over the wide range of cases observed in the clinical and screening practice (different types and stages of cancer, various benign tumors, different levels of tissue heterogeneity, etc.). *In vitro* optical studies of normal and diseased breast tissues have not found significant differences between their optical properties.<sup>109,110</sup> This result further suggests that the optical contrast induced by cancer may result only from modifications to the vascularization, oxygenation, or tissue architecture, which are significantly altered for the measurements *in vitro*. In fact, *in vivo* measurements have indicated that cancerous breast tissue has a significantly larger absorption coefficient and a marginally larger reduced scattering coefficient with respect to normal breast tissue.<sup>111-113</sup> Since it is yet to be demonstrated that optical mammography can rely solely on the intrinsic optical contrast associated with cancer, it has recently been proposed the use of dyes as optical contrast agents.<sup>73,114,115</sup>

The first clinical tests of breast transillumination for diagnostic purposes were performed by Cutler in 1929.<sup>116</sup> This approach was soon abandoned because of the poor sensitivity and specificity of the method. In the 70's and 80's, technical developments led to two new optical techniques called *diaphanography*<sup>117</sup> and *lightscanning*,<sup>118</sup> which induced a renewed enthusiasm for optical mammography. These approaches employed a broad beam of visible and NIR continuous wave (CW) light that illuminated one side of the breast. On the opposite side of the breast, the examiner visually inspected the light transmission pattern and used a video camera for image recording. The examination had to be performed in a dark room, and the examiner's eyes needed to be dark-adapted. Despite some encouraging initial results,<sup>119</sup> several clinical studies conducted in the late 80's have shown that diaphanography and lightscanning are inferior to x-ray mammography both as a screening and as a

clinical tool.<sup>120,121</sup> As a result, medical acceptance of diaphanography and lightscanning has been subdued.

The introduction of time-resolved methods for tissue imaging has yielded new instrumental tools for optical mammography. Furthermore, the application of the diffusion equation [Eq. (7.47)] provides a mathematical model that allows for a more rigorous approach to optical mammography with respect to the mainly empirical studies of the past. As a result, new time-domain<sup>73,112,122-124</sup> and frequency-domain<sup>18,105,113,125-128</sup> approaches for optical mammography have recently been developed. Siemens AG, Medical Engineering (Erlangen, Germany) has recently designed and clinically tested a frequency-domain prototype for optical mammography.<sup>129</sup> Figure 7.12 shows a block diagram of this prototype and two representative optical mammograms obtained on a patient affected by breast cancer. The optical mammograms shown in Fig. 7.12 are 2-D projection images obtained by scanning two collinear optical fibers (one for illumination, one for light collection) placed on the opposite sides of the slightly compressed breast. The total time required to scan the breast is 2-3 min. The frequency-domain optical data have been processed with an algorithm designed to enhance tumor contrast by minimizing the effects of the breast geometry on the optical data.<sup>80</sup> As in x-ray mammography, the breast is imaged in two directions, leading to a craniocaudal (cc) and an oblique (ob) view. Figure 7.12 shows that breast cancer can be detected with excellent contrast using optical methods. However, optical mammography still needs to improve its performance in the detection of small tumors and in the discrimination between malignant tumors and benign breast lesions. A preliminary analysis based on the criterion that an optical mammogram is positive if it shows a region of abnormal absorbance in both the craniocaudal and oblique views, has lead to a sensitivity (fraction of cancerous breasts successfully detected) of 72% and a specificity (fraction of non-cancerous breasts correctly evaluated as negative) of 52% on a clinical population of 131 patients.<sup>130</sup> This result is consistent with the sensitivity of 73% obtained on 69 patients<sup>131</sup> with a similar frequency-domain prototype developed independently by the research laboratories of Carl Zeiss (Oberkochen, Germany).<sup>132</sup> It must be stressed that these results, which are based on optical mammograms like the ones shown in Fig. 7.12(b), rely on 2-D projection data at a single wavelength. The potential of optical mammography goes beyond these capabilities, so that there are a number of possibilities for developing more effective approaches. For instance, testing non-planar geometries without (or with minimal) breast compression, exploiting the spectral information, quantifying and discriminating the breast absorption and scattering coefficients, achieving a true 2-D or 3-D spatial reconstruction of the breast optical properties, performing oxygenation or blood flow imaging, and developing imaging approaches based on dynamic perturbations (such as periodic light compression and decompression of the breast), are some of the areas currently under investigation by research groups worldwide.

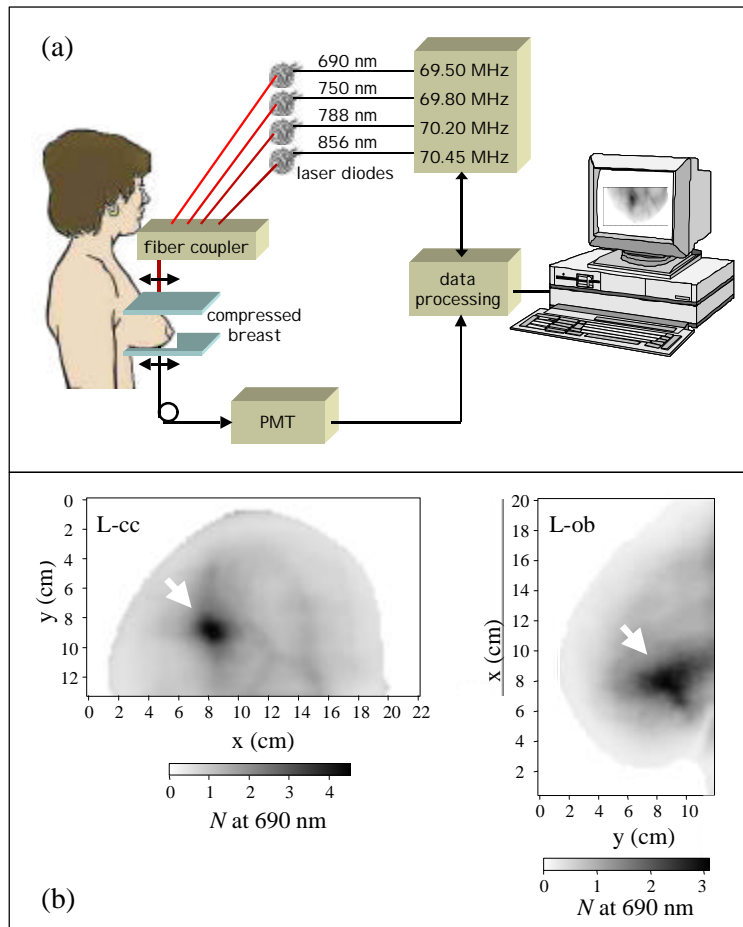


Fig. 7.12. (a) Schematic diagram of the prototype for frequency-domain (70 MHz) optical mammography developed by Siemens AG, Medical Engineering.<sup>129</sup> The slightly compressed breast is optically scanned to obtain 2-D projection images at four wavelengths (690, 750, 788, and 856 nm). The optical detector is a photomultiplier tube (PMT). The scanning time is about 2 min per image. The optical image of the breast is displayed in real-time during the examination. (b) Craniocaudal (cc) and oblique (ob) views of the left (L) breast of a 72 year old patient (patient No. 197) affected by invasive ductal carcinoma. Cancer size is 2.5 cm. The cancer, indicated by arrows, appears with high contrast in both views of the breast. The imaged parameter ( $N$  at 690 nm) is related to the optical absorbance of breast tissue,<sup>80</sup> so that the higher value of  $N$  at the cancer location indicates a higher optical absorption with respect to healthy tissue.

## 7.6 Future directions

The key difference between continuous-wave (CW) and frequency-domain spectroscopy is the phase measurement capability afforded by the frequency-

domain. For optical studies of tissues, the phase information can be exploited in at least two ways.

First, by combining the phase measurement with the DC intensity, AC amplitude, or modulation measurement, one can separately measure the absorption and the reduced scattering coefficients of tissues. This is of paramount importance for quantitative tissue spectroscopy, imaging, and oximetry. In this chapter, we have illustrated the capability of frequency-domain spectroscopy to quantify the absorption and the reduced scattering coefficients (Figs. 7.3(d), 7.5, and 7.9), and to perform absolute tissue oximetry (Figs. 7.6-7.8).

The second relevant aspect of the phase measurement is that the phase is sensitive to a different tissue volume with respect to the DC intensity and AC amplitude. The region of sensitivity can be evaluated by the effect on the measured quantities of a small perfectly absorbing object located at  $\mathbf{r}$ . In particular, the DC, AC, and phase sensitivities can be expressed by the parameters  $e_{DC}(\mathbf{r}) = DC(\mathbf{r})/DC_0$ ,  $e_{AC}(\mathbf{r}) = AC(\mathbf{r})/AC_0$ , and  $e_F(\mathbf{r}) = \Phi(\mathbf{r}) - \Phi_0$ , respectively, where  $DC_0$ ,  $AC_0$ ,  $\Phi_0$ , are the measured values in the absence of the absorbing object, and  $DC(\mathbf{r})$ ,  $AC(\mathbf{r})$ ,  $\Phi(\mathbf{r})$  are the measured values in the presence of the absorbing object at point  $\mathbf{r}$ . The theoretical and experimental regions of sensitivities for the DC, AC, and phase are illustrated in Fig. 7.13 for an infinite medium (other conditions are listed in the figure caption).<sup>133</sup> Figure 7.13 shows that the DC and AC measurement are most sensitive to the region along the line joining the source and the detector, which, by contrast, is not the highest region of sensitivity for the phase. In a non-invasive tissue measurement, which is better modeled by a semi-infinite geometry, where the illuminating and collecting optical fibers are located on the tissue/air interface, the phase measurement is typically less sensitive to the superficial tissue layer with respect to the DC and AC measurements. As a result, the phase information may contribute to achieving depth discrimination in optical imaging of tissues.

Future applications of frequency-domain techniques to the optical study of biological tissues will exploit the two above-mentioned features, with the objective of developing innovative approaches for medical imaging and diagnosis.

## Acknowledgments

We thank E. Gratton, B. Barbieri, and D. Hueber for useful discussions, and E. Heffer for the critical reading of the manuscript. This research is supported by the US National Institutes of Health (Grants No. CA57032 and MH62854) and by the US Department of the Army (Award No. DAMD17-99-1-9218).

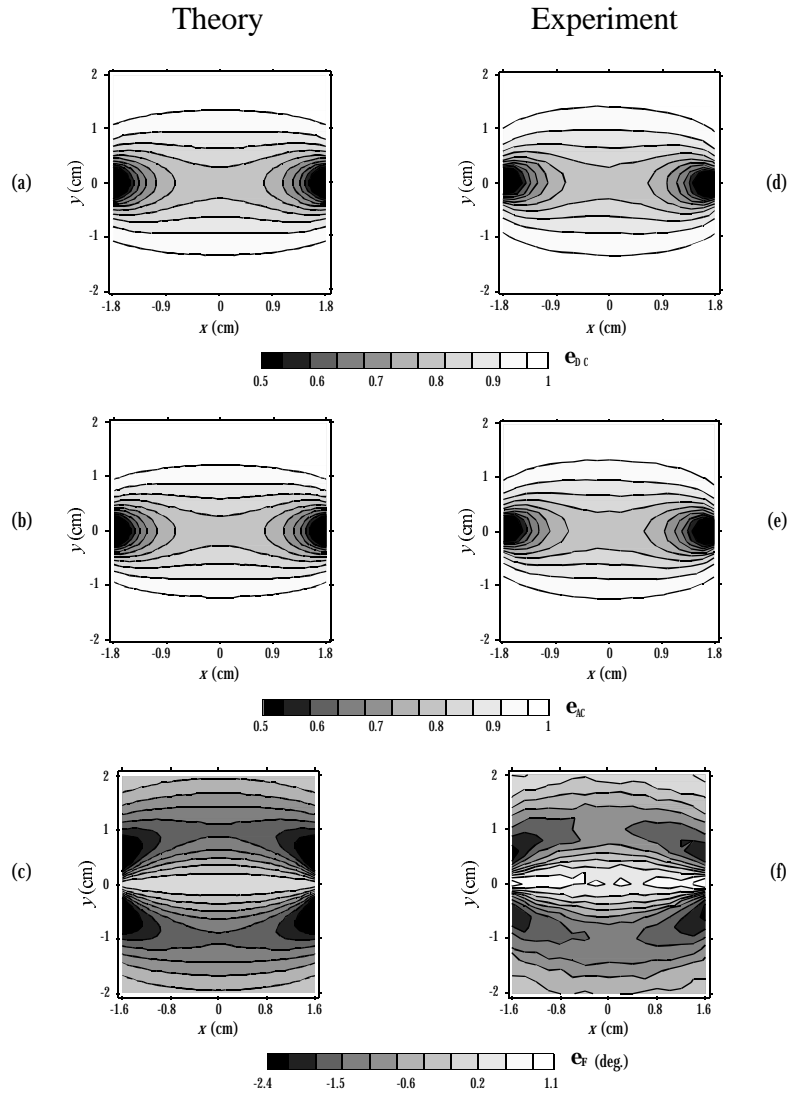


Fig. 7.13. Regions of sensitivity for the DC (panels (a) and (d)), AC (panels (b) and (e)), and phase (panels (c) and (f)) in an infinite medium. The source and the detector (not shown) are located respectively in  $(-2,0)$  and  $(2,0)$ . The optical properties of the medium are  $\mu_a = 0.03 \text{ cm}^{-1}$ ,  $\mu_s' = 19 \text{ cm}^{-1}$ , and the source modulation frequency is 120 MHz. The gray scales represent the parameters  $e_{DC}$ ,  $e_{AC}$ , and  $e_F$ , which are defined in the text. The left panels are theoretical predictions based on diffusion theory, while the right panels are experimental results.<sup>133</sup>

## References

1. D. T. Delpy, M. Cope, P. van der Zee, S. Arridge, S. Wray, and J. Wyatt, "Estimation of Optical Pathlength through Tissue from Direct Time of Flight Measurement," *Phys. Med. Biol.* **33**, 1433-1442 (1988).
2. M. S. Patterson, B. Chance, and B. C. Wilson, "Time Resolved Reflectance and Transmittance for the Non-Invasive Measurement of Optical Properties," *Appl. Opt.* **28**, 2331-2336 (1989).
3. B. Chance, M. Cope, E. Gratton, N. Ramanujam, and B. Tromberg, "Phase Measurement of Light Absorption and Scatter in Human Tissue," *Rev. Sci. Instrum.* **69**, 3457-3481 (1998).
4. E. Gratton and M. Limkeman, "A Continuously Variable Frequency-Domain Cross-Correlation Phase Fluorometer with Picosecond Resolution," *Biophys. J.* **44**, 315-324 (1983).
5. R. D. Spencer and G. Weber, "Measurement of Subnanosecond Fluorescence Lifetimes with a Cross-Correlation Phase Fluorometer," *Ann. N. Y. Acad. Sci.* **158**, 361-376 (1969).
6. D. W. Piston, G. Marriott, T. Radivoyevich, R. Clegg, T. M. Jovin, and E. Gratton, "Wide-Band Acousto-Optic Light Modulator for Frequency-Domain Fluorometry and Phosphorimetry," *Rev. Sci. Instrum.* **60**, 2596-2600 (1989).
7. J. R. Alcalá, E. Gratton, and D. M. Jameson, "A Multifrequency Phase Fluorometer Using the Harmonic Content of a Mode-Locked Laser," *Anal. Instrum.* **14**, 225-250 (1985).
8. E. Gratton, D. M. Jameson, N. Rosato, and G. Weber, "Multifrequency Cross-Correlation Phase Fluorometer Using Synchrotron Radiation," *Rev. Sci. Instrum.* **55**, 486-493 (1984).
9. G. De Stasio, N. Zema, F. Antonangeli, A. Savoia, T. Parasassi, and N. Rosato, "Plastique: A Synchrotron Radiation Beamline for Time Resolved Fluorescence in the Frequency Domain," *Rev. Sci. Instrum.* **62**, 1670-1671 (1991).
10. S. Fantini, M. A. Franceschini, J. B. Fishkin, B. Barbieri, and E. Gratton, "Quantitative Determination of the Absorption Spectra of Chromophores in Strongly Scattering Media: a Light-Emitting-Diode Based Technique," *Appl. Opt.* **33**, 5204-5213 (1994).
11. E. Gratton, W. W. Mantulin, M. J. van de Ven, and J. B. Fishkin, "A Novel Approach to Laser Tomography," *Bioimaging* **1**, 40-46 (1993).
12. A. Knüttel, J. M. Schmitt, and J. R. Knutson, "Spatial Localization of Absorbing Bodies by Interfering Diffusive Photon-Density Waves," *Appl. Opt.* **32**, 381-389 (1993).

13. E. M. Sevick, J. K. Frisoli, C. L. Burch, and J. R. Lakowicz, "Localization of Absorbers in Scattering Media by Use of Frequency-Domain Measurements of Time-Dependent Photon Migration," *Appl. Opt.* **33**, 3562-3570 (1994).
14. B. Guan, Y. Zhang, and B. Chance, "A New Multi-Wavelength Phase Modulation System for Photon Diffusion Studies," *Proc. SPIE* **2979**, 838-846 (1997).
15. J. R. Lakowicz and K. Berndt, "Frequency-Domain Measurements of Photon Migration in Tissues," *Chem. Phys. Lett.* **166**, 246-252 (1990).
16. J. B. Fishkin, S. Fantini, M. J. vandeVen, and E. Gratton, "Gigahertz Photon Density Waves in a Turbid Medium: Theory and Experiments," *Phys. Rev. E* **53**, 2307-2319 (1996).
17. S. J. Madsen, E. R. Anderson, R. C. Haskell, and B. J. Tromberg, "Portable, high-bandwidth frequency-domain photon migration instrument for tissue spectroscopy," *Opt. Lett.* **19**, 1934-1936 (1994).
18. X. D. Li, T. Durduran, A. G. Yodh, B. Chance, and D. N. Pattanayak "Diffraction tomography for biochemical imaging with diffuse-photon density waves," *Opt. Lett.* **22**, 573-575 (1997).
19. K. W. Berndt and J. R. Lakowicz, "Detection and Localozation of Absorbers in Scattering Media Using Frequency-Domain Principles," *Proc. SPIE* **1431**, 149-160 (1991).
20. T. E. French, "The Development of Fluorescence Lifetime Imaging and an Application in Immunology," Ph.D. Thesis, Dept. of Physics, University of Illinois at Urbana-Champaign, (1996).
21. B. A. Feddersen, D. W. Piston, and E. Gratton, "Digital Parallel Acquisition in Frequency Domain Fluorometry," *Rev. Sci. Instrum.* **60**, 2929-2936 (1989).
22. R. N. Bracewell, *The Fourier Transform and Its Applications*, (McGraw-Hill, Singapore, 1986), pp. 189-194.
23. S. Fantini, M. A. Franceschini, J. S. Maier, S. A. Walker, B. Barbieri, and E. Gratton, "Frequency-Domain Multichannel Optical Detector for non-Invasive Tissue Spectroscopy and Oximetry," *Opt. Eng.* **34**, 32-42 (1995).
24. M. A. Franceschini, E. Gratton, D. Hueber, and S. Fantini, "Near-Infrared Absorption and Scattering Spectra of Tissues *in Vivo*," *Proc. SPIE* **3597**, 526-531 (1999).
25. S. Fantini, M. A. Franceschini, and E. Gratton, "Semi-Infinite-Geometry Boundary Problem for Light Migration in Highly Scattering Media: a Frequency-Domain Study in the Diffusion Approximation," *J. Opt. Soc. Am. B* **11**, 2128-2138 (1994).
26. J. J. Duderstadt and L. J. Hamilton, *Nuclear Reactor Analysis*, (Wiley, New York, NY, 1976), p. 113.

27. F. Hetzel, M. Patterson, L. Preuss, and B. Wilson, "Recommended Nomenclature for Physical Quantities in Medical Applications of Light," AAPM Report No. 57, American Institute of Physics, Woodbury, NY, pp. 1-6 (1996).
28. J.-M. Kaltenbach and M. Kaschke, "Frequency- and Time-Domain Modelling of Light Transport in Random Media," in *Medical Optical Tomography: Functional Imaging and Monitoring*, Editors G. J. Muller *et al.*, (SPIE, Bellingham, Washington, 1993), pp. 65-86.
29. D. A. Boas, "Diffuse Photon Probes of Structural and Dynamical Properties of Turbid Media: Theory and Biomedical Applications," Ph.D. Thesis, Dept. of Physics, University of Pennsylvania, (1996).
30. S. R. Arridge, "Optical tomography in medical imaging," *Inverse Problems* **15**, R41-R93 (1999).
31. H. W. Wyld, *Mathematical Methods for Physics*, Addison-Wesley, Reading, MA, (1994), Chapter 3.
32. G. Zaccanti, E. Battistelli, P. Brusaglioni, and Q. Wei, "Analytic Relationships for the Statistical Moments of Scattering Point Coordinates for Photon Migration in a Scattering Medium," *Pure Appl. Opt.* **3**, 897-905 (1994).
33. D. A. Boas, M. A. O'Leary, B. Chance, and A. G. Yodh, "Scattering of Diffuse Photon Density Waves by Spherical Inhomogeneities within Turbid Media: Analytic Solution and Applications," *Proc. Natl. Acad. Sci. USA* **91**, 4887-4891 (1994).
34. J. B. Fishkin and E. Gratton, "Propagation of Photon-Density Waves in Strongly Scattering Media Containing an Absorbing Semi-Infinite Plane Bounded by a Straight Edge," *J. Opt. Soc. Am. A* **10**, 127-140 (1993).
35. R. C. Haskell, L. O. Svaasand, T. T. Tsay, T. C. Feng, M. S. McAdams, and B. J. Tromberg, "Boundary Conditions for the Diffusion Equation in Radiative Transfer," *J. Opt. Soc. Am. A* **11**, 2727-2741 (1994).
36. M. S. Patterson, J. D. Moulton, B. C. Wilson, K. W. Berndt, and J. R. Lakowicz, "Frequency-Domain Reflectance for the Determination of the Scattering and Absorption Properties of Tissue," *Appl. Opt.* **30**, 4474-4476 (1991).
37. S. R. Arridge, M. Cope, and D. T. Delpy, "The Theoretical Basis for the Determination of Optical Pathlengths in Tissue: Temporal and Frequency Analysis," *Phys. Med. Biol.* **37**, 1531-1560 (1992).
38. J. Ricka, "Dynamic Light Scattering with Single-Mode and Multimode Receivers," *Appl. Opt.* **32**, 2860-2875 (1993).
39. D. J. Pine, D. A. Weitz, P. M. Chaikin, and E. Herbolzheimer, "Diffusing-Wave Spectroscopy," *Phys. Rev. Lett.* **60**, 1134-1137(1988).

40. D. A. Boas and A. G. Yodh, "Spatially Varying Dynamical Properties of Turbid Media Probed with Diffusing Temporal Light Correlation," *J. Opt. Soc. Am. A* **14**, 192-215 (1997).
41. I. M. Braverman, "Anatomy and Physiology of the Cutaneous Microcirculation," in *Bioengineering of the Skin: Cutaneous Blood Flow and Erythema*, E. Berardesca, P. Elsner, and H. I. Maibach, Editors, (CRC Press, Boca Raton, FL, 1995).
42. G. M. Hale and M. R. Querry, "Optical Constants of Water in the 200 nm to 200  $\mu$ m Wavelength Region," *Appl. Opt.* **12**, 555-563 (1973).
43. S. Prahl (of the Oregon Medical Laser Center, Portland, OR) has tabulated the molar extinction coefficients for oxy-hemoglobin and deoxy-hemoglobin using data from W. B. Gratzer and N. Kollias. These tabulated data are available at <http://omlc.ogi.edu/spectra/hemoglobin/summary.html>.
44. W. F. Cheong, S. A. Prahl, and A. J. Welch, "A Review of the Optical Properties of Biological Tissues," *IEEE J. Quantum Electron.* **26**, 2166-2185 (1990).
45. Francis A. Duck, *Physical Properties of Tissues: A Comprehensive Reference Book* (Academic Press, San Diego, CA, 1990).
46. M. A. Franceschini, E. Gratton, and S. Fantini, "Non-Invasive Optical Method to Measure Tissue and Arterial Saturation: an Application to Absolute Pulse Oximetry of the Brain," *Opt. Lett.* **24**, 829-831 (1999).
47. G. A. Millikan, "The Oximeter, an Instrument for Measuring Continuously the Oxygen Saturation of Arterial Blood in Man," *Rev. Sci. Instr.* **13**, 434-444 (1942).
48. Y. Mendelson, "Pulse Oximetry: Theory and Applications for Noninvasive Monitoring," *Clin. Chem.* **38**, 1601-1607 (1992).
49. M. Miwa, Y. Ueda and B. Chance, "Development of Time Resolved Spectroscopy System for Quantitative Non-Invasive Tissue Measurement," *Proc. SPIE*, **2389**, 142-149 (1995).
50. V. Quaresima, M. A. Franceschini, S. Fantini, E. Gratton, and M. Ferrari, "Difference in Leg Muscles Oxygenation During Treadmill Exercise by a New Near Infrared Frequency-Domain Oximeter," in *Photon Propagation in Tissues III*, D. A. Benaron, B. Chance, M. Ferrari, Editors, *Proc. SPIE* **3194**, 116-120 (1998).
51. T. R. Cheatle, L. A. Potter, M. Cope, D. T. Delpy, P. D. Coleridge Smith, and J. H. Scurr, "Near-Infrared Spectroscopy in Peripheral Vascular Disease," *Br. J. Surg.* **78**, 405-408 (1991).
52. R. A. de Blasi, M. Cope, and M. Ferrari, "Oxygen Consumption of Human Skeletal Muscle by Near-Infrared Spectroscopy During Tourniquet-Induced Ischemia in Maximal Voluntary Contraction," *Adv. Exp. Med. Biol.* **317**, 771-777 (1992).

53. R. A. de Blasi, M. Ferrari, A. Natali, G. Conti, A. Mega, and A. Gasparetto, "NonInvasive Measurement of Forearm Blood Flow and Oxygen Consumption by Near-Infrared Spectroscopy," *J. Appl. Physiol.* **76**, 1388-1393 (1994).
54. S. Homma, H. Eda, S. Ogasawara, and A. Kagaya, "Near-Infrared Estimation of O<sub>2</sub> Supply and Consumption in Forearm Muscles Working at Varying Intensity," *J. Appl. Physiol.* **80**, 1279-1284 (1996).
55. M. C. P. van Beekvelt, W. N. J. M. Colier, B. G. M. van Engelen, M. T. E. Hopman, R. A. Wevers, and B. Oeseburg, "Validation of Measurement Protocols to Assess Oxygen Consumption and Blood Flow in the Human Forearm by Near-Infrared Spectroscopy," *Proc. SPIE* **3194**, 133-144 (1998).
56. C. Casavola, L. A. Paunescu, S. Fantini, and E. Gratton, "Blood Flow and Oxygen Consumption with Near-Infrared Spectroscopy and Venous Occlusion: Spatial Maps and the Effect of Time and Pressure of Inflation," *J. Biomed. Opt.* **5**, 269-276 (2000).
57. S. R. Hintz, D. A. Benaron, J. P. van Houten, J. L. Duckworth, F. W. H. Liu, S. D. Spilman, D. K. Stevenson, and W.-F. Cheong, "Stationary Headband for Clinical Time-of-Flight Optical Imaging at the Bedside," *Photochem. Photobiol.* **68**, 361-369 (1998).
58. S. R. Hintz, W.-F. Cheong, J. P. van Houten, D. K. Stevenson, and D. A. Benaron, "Bedside Imaging of Intracranial Hemorrhage in the Neonate Using Light: Comparison with Ultrasound, Computed Tomography, and Magnetic Resonance Imaging," *Pediatr. Res.* **45**, 54-59 (1999).
59. B. Beauvoit, T. Kitai, and B. Chance, "Contribution of the Mitochondrial Compartment to the Optical Properties of the Rat Liver: A Theoretical and Practical Approach," *Biophys. J.* **67**, 2501-2510 (1994).
60. M. Kohl, M. Cope, M. Essenpreis, and D. Böcker, "Influence of Glucose Concentration on Light Scattering in Tissue-Simulating Phantoms," *Opt. Lett.* **19**, 2170-2172 (1994).
61. J. S. Maier, S. A. Walker, S. Fantini, M. A. Franceschini, and E. Gratton, "Possible Correlation between Blood Glucose Concentration and the Reduced Scattering Coefficient of Tissues in the Near Infrared," *Opt. Lett.* **19**, 2062-2064 (1994).
62. J. T. Bruulsema, J. E. Hayward, T. J. Farrel, M. S. Patterson, L. Heinemann, M. Berger, T. Koschinsky, J. Sandahl-Christiansen, H. Orskov, M. Essenpreis, G. Schmelzeisen-Redeker, and D. Böcker, "Correlation Between Blood Glucose Concentration in Diabetics and Noninvasively Measured Tissue Optical Scattering Coefficient," *Opt. Lett.* **22**, 190-192 (1997).

63. V. V. Tuchin, I. L. Maksimova, V. I. Kochubei, I. L. Kon, A. H. Mavlutov, A. A. Mishin, S. V. Tuchin, and D. A. Zymnyakov, "Optical and Osmotic Properties of Human Sclera," *Proc. SPIE* **2979**, 658-675 (1997).
64. S. A. Walker, D. A. Boas, and E. Gratton, "Photon Density Waves Scattered from Cylindrical Inhomogeneities: Theory and Experiments," *Appl. Opt.* **37**, 1935-1944 (1998).
65. B. W. Pogue, M. S. Patterson, H. Jiang, and K. D. Paulsen, "Initial Assessment of a Simple System for Frequency Domain Diffuse Optical Tomography," *Phys. Med. Biol.* **40**, 1709-1729 (1995).
66. S. R. Arridge, M. Schweiger, M. Hiraoka, and D. T. Delpy, "A Finite Element Approach to Modelling Photon Transport in Tissue," *Med. Phys.* **20**, 299-309 (1993).
67. S. R. Arridge, P. van der Zee, M. Cope, and D. T. Delpy, "Reconstruction Methods for Infra-Red Absorption Imaging," *Proc. SPIE* **1431**, 204-215 (1991).
68. M. A. O'Leary, D. A. Boas, B. Chance, and A. G. Yodh, "Experimental Images of Heterogeneous Turbid Media by Frequency-Domain Diffusing Photon Tomography," *Opt. Lett.* **20**, 426-428 (1995).
69. L. H. Wang, S. L. Jacques, "Hybrid Model of Monte-Carlo Simulation and Diffusion Theory for Light Reflectance by Turbid media," *J. Opt. Soc. Am. A* **10**, 1746-1752 (1993).
70. I. V. Yaroslavsky, A. N. Yaroslavsky, H.-J. Schwarzmaier, G. G. Akchurin, and V. V. Tuchin, "A New Approach to Monte Carlo Simulation of Photon Transport in the Frequency Domain," *Proc. SPIE* **2626**, 45-55 (1995).
71. A. H. Gandjbakhche, R. F. Bonner, R. Nossal, and G. H. Weiss, "Absorptivity Contrast in Transillumination Imaging of Tissue Abnormalities," *Appl. Opt.* **35**, 1767-1774 (1996).
72. H. L. Graber, J. Chang, J. Lubowsky, R. Aronson, and R. L. Barbour, "Near-Infrared Absorption Imaging of Dense Scattering Media by Steady-State Diffusion Tomography," *Proc. SPIE* **1888**, 372-386 (1993).
73. V. Ntziachristos, A. G. Yodh, M. Schnall, and B. Chance, "Concurrent MRI and Diffuse Optical Tomography of Breast after Indocyanine Green Enhancement," *Proc. Natl. Acad. Sci. USA* **97**, 2767-2772, (2000).
74. S. R. Arridge, M. Schweiger, M. Hiraoka, and D. T. Delpy, "Performance of an Iterative Reconstruction Algorithm for Near-Infrared Absorption Imaging," *Proc. SPIE* **1888**, 360-371 (1993).
75. H. Jiang, K. D. Paulsen, U. L. Osterberg, B. W. Pogue, and M. S. Patterson, "Simultaneous Reconstruction of Optical Absorption and Scattering Maps in Turbid Media from Near-Infrared Frequency-Domain Data," *Opt. Lett.* **20**, 2128-2130 (1995).

76. B. W. Pogue, T. O. McBride, J. Prewitt, U. L. Österberg, and K. D. Paulsen, "Spatially Variant Regularization Improves Diffuse Optical Tomography," *Appl. Opt.* **38**, 2950-2961 (1999).
77. D. A. Benaron, D. C. Ho, S. Spilman, J. P. Van Houten, and K. D. Stevenson, "Non-recursive linear algorithms for optical imaging in diffusive media," *Adv. Exp. Med. Biol.* **361**, 215-222 (1994).
78. S. A. Walker, S. Fantini, and E. Gratton, "Image Reconstruction Using Back-Projection from Frequency-Domain Optical Measurements in Highly Scattering Media," *Appl. Opt.* **36**, 170-179 (1997).
79. M. A. Franceschini, V. Toronov, M. E. Filiaci, E. Gratton, and S. Fantini, "On-Line Optical Imaging of the Human Brain with 160-ms Temporal Resolution," *Opt. Express* **6**, 49-57 (2000).
80. S. Fantini, M. A. Franceschini, and E. Gratton, "Effective Source Term in the Diffusion Equation for Photon Transport in Turbid Media," *Appl. Opt.* **36**, 156-163 (1997).
81. F. F. Jöbsis "Noninvasive, infrared monitoring of cerebral and myocardial oxygen sufficiency and circulatory parameters," *Science* **198**, 1264-1267 (1977).
82. P. W. McCormick, M. Stewart, G. Lewis, M. Dujovny, and J. I. Ausman, "Intracerebral Penetration of Infrared Light. Technical note," *J. Neurosurg.* **76**, 315-318 (1992).
83. G. Gratton, J. S. Maier, M. Fabiani, W. W. Mantulin, and E. Gratton, "Feasibility of intracranial near-infrared optical scanning," *Psychophysiology* **31**, 211-215 (1994).
84. S. P. Gopinath, C. S. Robertson, R. G. Grossman, and B. Chance, "Near-Infrared Spectroscopic Localization of Intracranial Hematomas," *J. Neurosurg.* **79**, 43-47 (1993).
85. S. Fantini, M. A. Franceschini, E. Gratton, D. Hueber, W. Rosenfeld, D. Maulik, P. G. Stubblefield, and M. R. Stankovic, "Non-invasive optical mapping of the piglet brain in real time," *Opt. Express* **4**, 308-314 (1999).
86. C. S. Roy and C. S. Sherrington, "On the Regulation of the Blood Supply of the Brain," *J. Physiol.* **11**, 85-108 (1890).
87. A. Villringer, and U. Dirnagl, "Coupling of Brain Activity and Cerebral Blood Flow: Basis of Functional Neuroimaging," *Cerebrovasc. Brain Metab. Rev.* **7**, 240-276 (1995).
88. B. M. Salzberg and A. L. Obaid, "Optical Studies of the Secretory Event at Vertebrate Nerve Terminals," *Exp. Biol.* **139**, 195-231 (1988).
89. R. A. Stepanoski, A. LaPorta, F. Raccuia-Behling, G. E. Blonder, R. E. Slusher, and D. J. Kleinfeld, "Noninvasive Detection of Changes in Membrane Potential in Cultured Neurons by Light Scattering," *Proc. Natl. Acad. Sci. USA* **88**, 9382-9386 (1991).

90. G. Gratton, P. M. Corballis, E. Cho, M. Fabiani, and D. C. Hood, "Shades of Gray Matter: Noninvasive Optical Images of Human Brain Responses During Visual Stimulation," *Psychophysiology* **32**, 505-509 (1995).
91. Y. Hoshi, H. Onoe, Y. Watanabe, J. Andersson, M. Bergstrom, A. Lilja, B. Langsrom, and M. Tamura, "Non-synchronous behavior of neuronal activity, oxidative metabolism and blood supply during mental tasks in man," *Neurosci. Lett.* **172** 129-133 (1994).
92. K. Villringer, A. Villringer, S. Minoshima, S. Ziegler, M. Herz, S. Schuh-Hofer, H. Obrig, C. Hock, U. Dirnagl, and M. Schwaiger, "Frontal Brain Activation in Humans: a Combined Near Infrared Spectroscopy and Positron Emission Tomography Study," *Soc. Neurosci. Abst.* **120**, 1 355 (1994).
93. S. Punwani, C. E. Cooper, M. Clemence, J. Pernice, P. Amess, J. Thornton, and R. J. Ordidge, "Correlation between Absolute Deoxyhaemoglobin [dHb] Measured by Near Infrared Spectroscopy (NIRS) and Absolute R2' as Determined by Magnetic Resonance Imaging (MRI)," *Adv. Exp. Med. Biol.* **413**, 129-137 (1997).
94. C. Hirth, K. Villringer, A. Thiel, J. Bernarding, W. Mühlnickl, H. Obrig, U. Dirnagl, and A. Villringer, "Towards Brain Mapping Combining Near-Infrared Spectroscopy and High Resolution 3D MRI," *Adv. Exp. Med. Biol.* **413**, 139-147 (1997).
95. A. Villringer, "Functional Neuroimaging Optical Approaches," *Adv. Exp. Med. Biol.* **413**, 1-18 (1997).
96. A. Maki, Y. Yamashita, Y. Ito, E. Watanabe, Y. Mayanagi, and H. Koizumi, "Spatial and Temporal Analysis of Human Motor Activity Using Noninvasive NIR Topography," *Med. Phys.* **22**, 1997-2005 (1995).
97. A. M. Siegel, J. J. A. Marota, and D. Boas, "Design and Evaluation of a Continuous-Wave Diffuse Optical Tomography System," *Opt. Express* **4**, 287-298 (1999).
98. B. Chance, E. Anday, S. Nioka, S. Zhou, L. Hong, K. Worden, C. Li, T. Murray, Y. Ovetsky, D. Pidikiti, and R. Thomas, "A Novel Method for Fast Imaging of Brain Function, Non-Invasively, with Light," *Opt. Express* **2**, 411-423 (1998).
99. R. M. Danen, Y. Wang, X. D. Li, W. S. Thayer, and A. G. Yodh, "Regional Imager for Low-Resolution Functional Imaging of the Brain with Diffusing Near-Infrared Light," *Photochem. Photobiol.* **67**, 33-40 (1998).
100. Y. Shinohara, M. Haida, N. Shinohara, F. Kawaguchi, Y. Itoh, and H. Koizumi, "Towards Near-Infrared Imaging of the Brain," *Adv. Exp. Med. Biol.* **413**, 85-89 (1997).
101. H. Koizumi, Y. Yamashita, A. Maki, T. Yamamoto, Y. Ito, H. Itagaki, and R. Kennan, "Higher-Order Brain Function Analysis by Trans-Cranial

- Dynamic Near-Infrared Spectroscopy Imaging,” *J. Biomed. Opt.* **4**, 403-413 (1999).
102. A. Villringer and B. Chance, “Non-Invasive Optical Spectroscopy and Imaging of Human Brain Function,” *Trends Neurosci.* **20**, 435-442 (1997).
  103. G. Gratton, M. Fabiani, D. Friedman, M. A. Franceschini, S. Fantini, P. M. Corballis, and E. Gratton, “Rapid Changes of Optical Parameters in the Human Brain During a Tapping Task,” *J. Cognitive Neuroscience* **7**, 446-456 (1995).
  104. K. A. Kang, D. F. Bruley, and B. Chance, “Feasibility Study of a Single- and Multiple-Source Near-Infrared Phase-Modulation Device for Characterizing Biological Systems,” *Biomed. Instrum. Technol.* **31**, 373-386 (1997).
  105. B. J. Tromberg, O. Coquoz, J. B. Fishkin, T. Pham, E. R. Anderson, J. Butler, M. Cahn, J. D. Gross, V. Venugopalan, and D. Pham, “Non-Invasive Measurements of Breast Tissue Optical Properties Using Frequency-Domain Photon Migration,” *Phil. Trans. R. Soc. Lond. B* **352**, 661-668 (1997).
  106. V. Quaresima, S. J. Matcher, and M. Ferrari, “Identification and Quantification of Intrinsic Optical Contrast for Near-Infrared Mammography,” *Photochem. Photobiol.* **67**, 4-14 (1998).
  107. S. Thomsen and D. Tatman, “Physiological and Pathological Factors of Human Breast Disease that Can Influence Optical Diagnosis,” *Ann. NY Acad. Sci.* **838**, 171-193 (1998).
  108. P. Vaupel, F. Kallinowski, and P. Okunieff, “Blood Flow, Oxygen and Nutrient Supply, and Metabolic Microenvironment of Human Tumors: A Review,” *Cancer Res.* **49**, 6449-6465 (1989).
  109. V. G. Peters, D. R. Wyman, M. S Patterson, and G. L. Frank, “Optical Properties of Normal and Diseased Human Breast Tissues in the Visible and Near-Infrared,” *Phys. Med. Biol.* **35**, 1317-1334 (1990).
  110. T. L. Troy, D. L. Page, and E. Sevick-Muraca, “Optical Properties of Normal and Diseased Breast Tissues: Prognosis for Optical Mammography,” *J. Biomed. Opt.* **1**, 342-355 (1996).
  111. S. Fantini, S. A. Walker, M. A. Franceschini, M. Kaschke, P. M. Schlag, and K. T. Moesta, “Assessment of the Size, Position, and Optical Properties of Breast Tumors *in Vivo* by Non-Invasive Optical Methods,” *Appl. Opt.* **37**, 1982-1989 (1998).
  112. D. Grosenick, H. Wabnitz, H. H. Rinneberg, K. T. Moesta, and P. M. Schlag, “Development of a Time-Domain Optical Mammograph and First *in vivo* Applications,” *Appl. Opt.* **38**, 2927-2943 (1999).

113. B. J. Tromberg, N. Shah, R. Lanning, A. Cerussi, J. Espinoza, T. Pham, L. Svaasand, and J. Butler, "Non-Invasive *In Vivo* Characterization of Breast Tumors Using Photon Migration Spectroscopy," *Neoplasia* **2**, 26-40 (2000).
114. B. Riefke, K. Licha, and W. Semmler, "Contrast Media for Optical Mammography," *Radiologe* **37**, 749-755 (1997).
115. S. Nioka, S. B. Colak, X. Li, Y. Yang, and B. Chance, "Breast Tumor Images of Hemodynamic Information Using a Contrast Agent with Back Projection and FFT Enhancement," *OSA Trends in Optics and Photonics Vol. 21, Advances in Optical Imaging and Photon Migration*, J. G. Fujimoto and M. S. Patterson, eds. (Optical Society of America, Washington, DC 1998), pp. 266-270.
116. M. Cutler, "Transillumination of the Breast," *Surg. Gynecol. Obstet.* **48**, 721-727 (1929).
117. C. M. Gros, Y. Quenneville, Y. Hummel, "Diaphanologie Mammaire," *J. Radiol. Electrol. Med. Nucl.* **53**, 297-306 (1972).
118. E. Carlsen, "Transillumination Light Scanning," *Diagn. Imaging* **4**, 28-34 (1982).
119. R. J. Bartrum and H. C. Crow, "Transillumination Lightscanning to Diagnose Breast Cancer: a Feasibility Study," *AJR* **142**, 409-414 (1984).
120. E. A. Sickles, "Breast Cancer Detection with Transillumination and Mammography," *AJR* **142**, 841-844 (1984).
121. A. Alverdy *et al.*, "Lightscanning Versus Mammography for the Detection of Breast Cancer in Screening and Clinical Practice," *Cancer* **65**, 1671-1677 (1990).
122. K. Wells, J. C. Hebden, F. E. W. Schmidt, and D. T. Delpy, "The UCL Multichannel Time-Resolved System for Optical Tomography," *Proc. SPIE* **2979**, 599-607 (1997).
123. V. Ntziachristos, X. H. Ma, and B. Chance, "Time-Correlated Single Photon Counting Imager for Simultaneous Magnetic Resonance and Near-Infrared Mammography," *Rev. Sci. Instrum.* **69**, 4221-4233 (1998).
124. R. Cubeddu, A. Pifferi, P. Taroni, A. Torricelli, and G. Valentini, "Noninvasive Absorption and Scattering Spectroscopy of Bulk Diffusive Media: An Application to the Optical Characterization of Human Breast," *Appl. Phys. Lett.* **74**, 874-876 (1999).
125. M. A. Franceschini, K. T. Moesta, S. Fantini, G. Gaida, E. Gratton, H. Jess, W. W. Mantulin, M. Seeber, P. M. Schlag, and M. Kaschke, "Frequency-Domain Techniques Enhance Optical Mammography: Initial Clinical Results," *Proc. Natl. Acad. Sci. USA* **94**, 6468-6473 (1997).
126. S. Zhou, C. Xie, S. Nioka, H. Liu, Y. Zhang, and B. Chance, "Phased Array Instrumentation Appropriate to High Precision Detection and Localization of Breast Tumor," in *Optical Tomography and Spectroscopy of Tissue:*

- Theory, Instrumentation, Model, and Human Studies II*, B. Chance and R. R. Alfano, eds., Proc. SPIE **2979**, 98-106 (1997).
127. B. W. Pogue, M. Testorf, T. McBride, U. Osterberg, and K. Paulsen, "Instrumentation and Design of a Frequency-Domain Diffuse Optical Tomography Imager for Breast Cancer Detection," *Opt. Expr.* **1**, 391-403 (1997).
  128. K. T. Moesta, S. Fantini, H. Jess, S. Totkas, M. A. Franceschini, M. Kaschke, and P. M. Schlag, "Contrast Features of Breast Cancer in Frequency-Domain Laser Scanning Mammography," *J. Biomed. Opt.* **3**, 129-136 (1998).
  129. L. Götz, S. H. Heywang-Köbrunner, O. Schütz, and H. Siebold, "Optische Mammographie an Präoperativen Patientinnen," *Akt. Radiol.* **8**, 31-33 (1998).
  130. S. Fantini, E. L. Heffer, M. A. Franceschini, L. Götz, A. Heinig, S. Heywang-Köbrunner, Oliver Schütz, and Horst Siebold, "Optical Mammography with Intensity-Modulated Light," Proceedings Volume from In Vivo Optical Imaging Workshop (September 16-17, 1999, National Institutes of Health, Bethesda, MD), A. Gandjbakhche, Ed. (Optical Society of America 2000), *in press*.
  131. H. Jess, H. Erdl, K. T. Moesta, S. Fantini, M. A. Franceschini, E. Gratton, and M. Kaschke, "Intensity-Modulated Breast Imaging: Technology and Clinical Pilot Study Results," *OSA Trends in Optics and Photonics on Advances in Optical Imaging and Photon Migration*, R. R. Alfano and J. G. Fujimoto, eds. (Optical Society of America, Washington, DC 1996), Vol. 2, pp. 126-129.
  132. M. Kaschke, H. Jess, G. Gaida, J. M. Kaltenbach, and W. Wrobel, "Transillumination Imaging of Tissue by Phase Modulation Techniques," in *Advances in Optical Imaging and Photon Migration*, Editor R. R. Alfano, Proc. OSA **21**, 88-92 (1994).
  133. S. Fantini, M. A. Franceschini, S. A. Walker, J. S. Maier, and E. Gratton, "Photon Path Distributions in Turbid Media: Applications for Imaging," Proc. SPIE **2389**, 340-349 (1995).